High Time Resolution Spectroscopic Measurements of Electron Temperature in the SSX plasma

Vernon H. Chaplin

(3/19/07)

Advisors: David H. Cohen, Michael R. Brown, Chris D. Cothran

Department of Physics & Astronomy
Swarthmore College
2007

Abstract

We present 1 μs time resolution calculations of the electron temperature of the Swarthmore Spheromak Experiment (SSX) plasma during magnetic reconnection. The non-LTE excitation kinematics code PrismSPECT is used to simulate emission spectra for a variety of plasma conditions. These model spectra are compared to experimental data from two main diagnostics: a vacuum ultraviolet (VUV) monochromator and a low-resolution soft x-ray detector (SXR). Analysis of simulation results reveals that the plasma quickly ($<$ 10 μs) approaches equilibrium conditions in the density regime of interest; as a result we can safely use steady-state simulations for comparisons with the data. Measured UV line strength ratios depend primarily on the electron temperature in the plasma, so we are able to use measurements of carbon impurity emission lines in conjunction with SXR measurements as a temperature diagnostic. In particular, the C III 97.7 nm / C IV 155 nm line intensity ratio proves to be extremely useful, while the C III 229.7 nm line appears anomalously strong in experimental measurements. Measurements of oxygen and nitrogen lines allow us to conclude that the carbon/oxygen number ratio in SSX is approximately 1000/1, while nitrogen concentrations are negligible. Temperatures derived from the 97.7 nm / 155 nm line ratio average 20 eV for single spheromak shots and 20 eV early in counter-helicity shots, increasing to 35 eV after the two spheromaks merge. SXR measurements suggest a mean electron temperature of 30-35 eV for single spheromak shots and 40 eV for counter-helicity merging. The counter-helicity temperature profile shows a distinct peak at t $\sim$40 μs, the time at which reconnection is believed to occur; however, the timing of this peak is not in precise agreement with the peak in the average temperature profile derived from carbon line ratios.

Contents

1. Introduction

1.1. Plasmas

1.1.1. What is Plasma?

Although relatively rare on Earth, material in the plasma state accounts for much of the matter in the universe, including stellar interiors and atmospheres, gaseous nebulae, and much of the interstellar medium. Studying plasmas is therefore crucial for our understanding of a multitude of astrophysical phenomena. A defining characteristic of plasmas is that they contain charged particles and therefore are readily influenced by electromagnetic forces. The need for charged particles explains their relative scarcity on Earth: at the low temperatures and high densities that we experience in everyday life, the fraction of atoms that are ionized is vanishingly small. F. F. Chen (6) provides a more formal definition: "A plasma is a quasineutral gas of charged and neutral particles which exhibits collective behavior."

Further explanation is required for several of these terms. Collective behavior means that the motions of particles in a plasma depend not only on local conditions but on plasma properties in remote regions as well. In an ordinary gas made up of neutral molecules, particle trajectories are affected only by collisions with other particles, and as a result the behavior of a gas molecule is influenced only by its nearest neighbors. In a plasma, on the other hand, each ion or electron creates electric and magnetic fields as it moves, while at the same time feeling the influence of the fields created by every other particle (6). This dynamic interaction is what makes the study of plasmas fascinating but also challenging.

Quasineutrality refers to the absence of large-scale electrostatic fields in plasmas. If one were to insert a positively charged object into a neutral gas, its electric field

would be felt everywhere in the gas with a strength proportional to one over the distance to the object squared. In a plasma, on the other hand, free electrons quickly surround the concentration of positive charge, thereby shielding its influence on the rest of the plasma through their own electric fields. The approximate length scale over which the electrostatic influence of a charged object can be felt is given by the Debye length, λ_D (equal to $\sim$1 μm in SSX). Using Poisson's equation ($\nabla^2\phi = -\rho/\epsilon_0$), it can be shown (6) that the potential falls off with increasing distance r from the body as

$$\phi \propto exp\,(r/\lambda_D) \tag{1.1}$$

where

$$\lambda_D = \left(\frac{\epsilon_0 k T_e}{n_e e^2}\right)^{1/2} \tag{1.2}$$

where k is Boltzmann's constant, T_e is the electron temperature in the plasma, and n_e is the average electron density. These quantities must be used because it is electrons and not ions that act as the primary shielding agents in most plasmas, due to their lower mass and greater mobility. In a plasma containing several species of particle (e.g. electrons and several types of ions), the temperature of each species may not be the same, and although they will eventually come to thermal equilibrium, the time scale on which this occurs may be longer than the lifetime of the plasma. As a result, we will often refer to T_e and T_i as separate quantities. As a final note, plasma physicists like to express temperatures in units of energy (kT) instead of T, so from this point forward temperatures will be given in electron volts (1 eV $\approx$ 11600 K).

1.1.2. Magnetic Reconnection

There is no mechanism analogous to Debye shielding for magnetic fields in plasmas, and as a result magnetic forces play a central role in determining plasma dy-

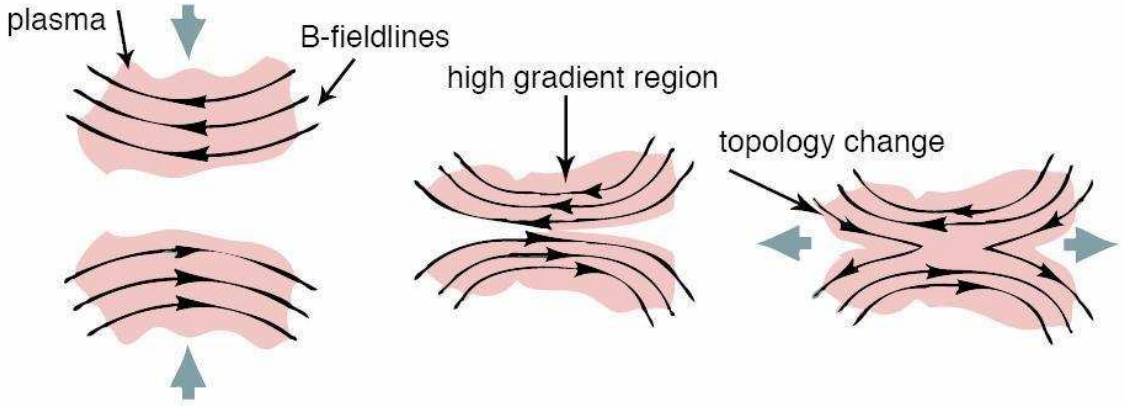

Fig. 1.— Schematic of magnetic reconnection. Black arrows represent magnetic field lines, and large blue arrows show flow velocities. In a perfectly conducting plasma, field lines are confined to move with the plasma. However, in real plasmas with finite resistivity, it is possible for field lines to diffuse through the plasma and reconnect. Figure from (24).

namics. The motion of a particle with charge q moving with velocity $\mathbf{v}$ in a magnetic field $\mathbf{B}$ is described by the Lorentz force law: $\mathbf{F} = q(\mathbf{v} \times \mathbf{B})$. Thus particles only feel a force in directions perpendicular to their velocities, and magnetic forces do no work but merely deflect particles along circular trajectories (13). Electrons and ions in a plasma will therefore tend to spiral along magnetic field lines, with the result that field lines move along with the bulk plasma flow patterns.

When two plasma components with oppositely directed magnetic fields collide, high field gradients develop at the interface between them. When $\frac{\partial \mathbf{B}}{\partial \mathbf{r}}$ becomes high enough, field lines can diffuse through the plasma, change their topology, and reconnect (see Figure 1). During reconnection, stored magnetic energy is converted to kinetic energy and heat, causing jets of plasma to flow out of the reconnection region and leading to increased temperatures. A more detailed description of magnetic reconnection will be presented in Chapter 2, but for now it suffices to say that reconnection is a complex process whose mysteries physicists are still unraveling through

astrophysical observations, laboratory experiments, and computer simulations.

1.1.3. Applications to Solar Physics

Although it may appear rather stable and uninteresting to the casual observer, the surface of the sun is in fact a complex and variable environment whose dynamics are controlled in large part by the presence of magnetic fields (44). A prominent phenomenon influenced by magnetic interactions in plasmas is solar flares–highly energetic bursts of photons, ions, and electrons ejected from the sun's outer atmosphere. Flares can effect the performance of weather and communications satellites, disrupt the earth's magnetic field, and in rare instances, even influence life on the ground. The Great Quebec Blackout on March 13, 1989 was caused by a large solar flare, as rapid changes in the geomagnetic field induced strong electric fields in Canadian power distribution grids (changing magnetic fields create electric fields through Faraday's law: $-\frac{\partial \mathbf{B}}{\partial t} = \nabla \times \mathbf{E}$) (1).

The mechanism through which solar flares are produced may be understood through an analogy to an earthquake. Prior to an earthquake, stress and energy build up through the relative motion of two tectonic plates along fault lines. At some point the stress becomes too great for the plates to move any further, and a section of the fault line snaps back into its original position (a minimum energy state). The excess energy is released in the form of kinetic energy and propogated as seismic waves. Similarly, solar flares occur when two magnetic regions of opposite polarity slide along a neutral line between them. As field lines become sheared, the stored magnetic energy increases. Eventually the configuration becomes unstable, and an "earthquake" occurs, releasing the energy that powers solar flares. This "earthquake" is magnetic reconnection (44).

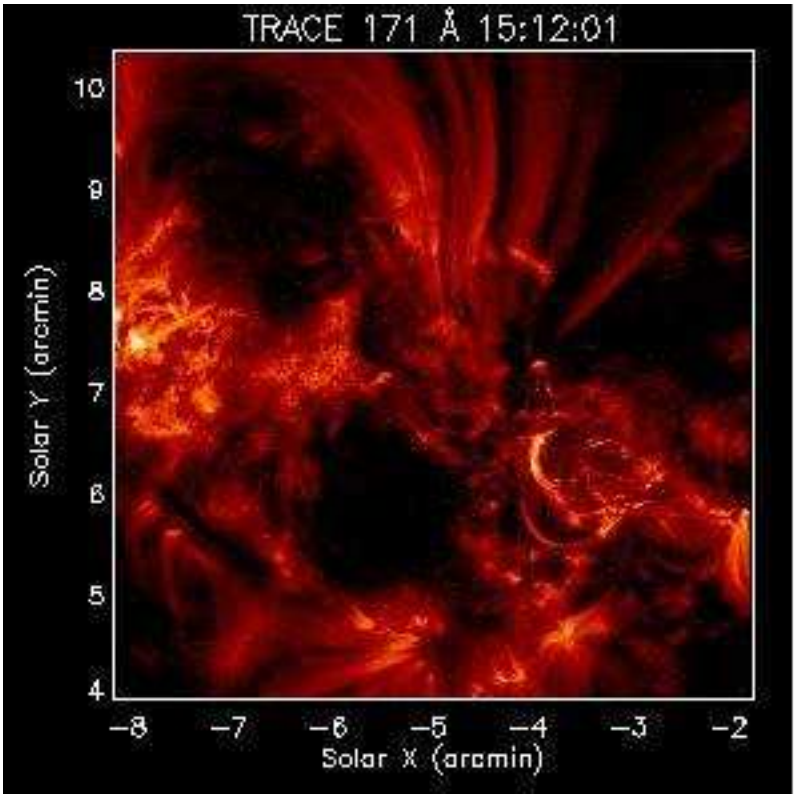

Fig. 2.— Loops of plasma rise above the surface of the sun during a solar flare. Image taken on March 27, 2001 during 17.1 nm observations by the TRACE (Transition Region and Coronal Explorer) satellite. Figure from http://trace.lmsal.com.

Reconnection is also suspected to be the primary mechanism behind the heating of the solar corona. The corona is the outermost layer of the sun's atmosphere, lying above the photosphere, from which most of the sun's visible light is emitted, and the chromosphere. Due to its low density (around 10^{10} m^{-3}), visible emission from the corona is dominated by light from the photosphere, and it can only be seen with the naked eye during a solar eclipse. Furthermore, it turns out that the peak wavelength of emission from the corona is not in the visible part of the spectrum at all, as the corona's temperature is around 170 eV (2×10^6 K). For much of the twentieth century, this temperature posed a great mystery to astronomers, because the average temperature of the photosphere is only about 0.5 eV (5500 K) (23).

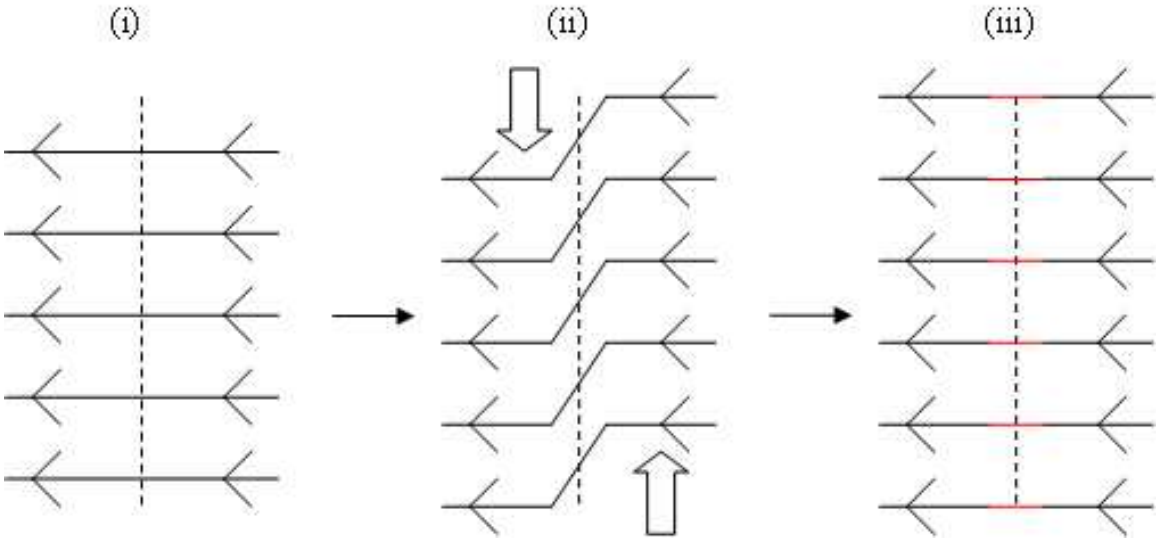

Fig. 3.— Solar flare creation through magnetic field line shearing. (a) Initially, field lines are directly connected across the neutral line dividing two magnetic regions of opposite polarity. (ii) As the regions slide along the neutral line, field lines become sheared, increasing the magnetic energy stored in the configuration. (iii) Extreme shearing leads to instabilities, allowing field lines to break and reconnect. Energy is released in the form of solar flares.

It makes very little sense intuitively that the layer furthest from the sun's core could maintain a temperature several hundred times hotter than that of the layer below it. In recent years, however, plasma physicists realized that the energy necessary to heat the corona could come from magnetic reconnection. The process through which this could happen is as follows: observations of the sun tell us that coronal magnetic field lines leave or return to the photosphere. Plasma in the photosphere moves about somewhat randomly, carrying with it the foot points of these field lines, so that the lines in the corona become more and more twisted. As stress on the system increases, so does the stored magnetic energy. This process cannot continue without bound–eventually the field lines will diffuse and reconnect, releasing the stored energy as heat (see Figure 3) (22). Because of the corona's low density, energy injected from reconnection can produce the extremely high temperatures seen.

The problem of coronal heating has by no means been solved; other heating mechanisms have also been proposed, and several have strong backing in the solar physics community. One such mechanism is the outward transfer of energy by acoustic or magnetic waves (see Chapter 2 for a more detailed discussion of waves in plasmas) (32). The subject is controversial in part because of the difficulty of verifying any of the coronal heating theories observationally. The relevant physical processes, such as the "nanoflares" proposed to contribute to matgnetic reconnection heating, occur on relatively small spatial scales; as a result, distinguishing one heating mechanism from another is beyond the capabilities of current observational technology (21). Therefore, laboratory plasma experiments and computer simulations will play a vital role in resolving the issue. Research at the Swarthmore Spheromak Experiment (SSX) focuses on the heating and bulk flows that are produced by the release of magnetic energy during reconnection. Measurements of properties such as the temperature increase during reconnection will help to address the plausability of reconnection as a primary mechanism for coronal heating.

1.2. Swarthmore Spheromak Experiment

SSX was designed to study magnetic reconnection events similar to those observed on the sun. The following sections describe the plasma configuration known as the spheromak and explain how spheromaks are created and used to study reconnection in SSX.

1.2.1. Plasma Confinement

One of the primary challenges in laboratory plasma research, both in astrophysical and fusion energy contexts, is how to achieve stable plasma confinement. Solid containers are obviously not a viable option, as no known material can withstand >10 eV temperatures without being damaged. For small concentrations of plasma, short-lived inertial confinement can be achieved through the use of powerful lasers, and investigations of this method form an important subfield in the area of fusion research. However, the simplest and most practical method for confining plasmas in the laboratory is to take advantage of the electromagnetic properties of ionized gases.

It might seem that plasma could be confined indefinitely in a carefully constructed electrostatic bottle. Recall, however, the property of quasineutrality–due to the conductive nature of plasmas, large-scale electrostatic fields are entirely damped out through the movements of free electrons. Furthermore, a result known as Earnshaw's theorem states that no stable configuration exists under purely electrostatic forces for ANY arrangement of charges. This theorem can be easily proved by invoking Gauss's law (13).

Fortunately for the state of laboratory plasma research, stable configurations ARE possible for moving particles under the influence of magnetic forces. One such stable configuration is a spheromak (see figure 4). The conditions necessary for stability will be discussed in Chapter 2; for now it is sufficient to say that a spheromak is a donut-shaped plasma structure that relaxes to a stable equilibrium within a simple container (i.e. a container that is topologically equivalent to a sphere). While other common plasma configurations such as the tokamak rely on externally applied magnetic fields, the spheromak is confined entirely by fields produced by its own internal currents. Spheromaks can be either "left-handed" or "right-handed;"; the distinction

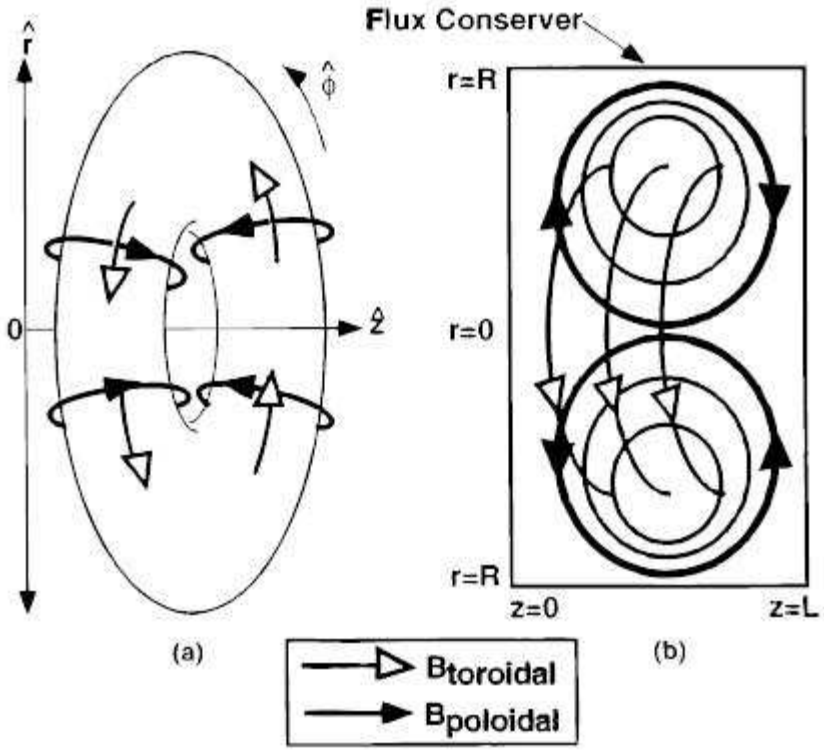

Fig. 4.— Two views of the magnetic field structure in a spheromak. Poloidal field lines pass through the hole of the "donut," while toroidal field lines circle the spheromak azimuthally. The spheromak shown is a left-handed spheromak. Figure from (11).

refers to the relative orientation of the toroidal and poloidal magnetic fields.

1.2.2. Spheromak Formation in SSX

Spheromaks in SSX are formed in coaxial plasma guns at either end of the main vacuum chamber (see Figure 5). The vacuum chamber is a stainless steel cylinder approximately 1 m long and 0.3 m in radius. Inside the chamber, there are a pair of cylindrical copper containers known as flux conservers that provide the conducting boundary for the spheromak fields. These have a radius of 0.2 m and a total length

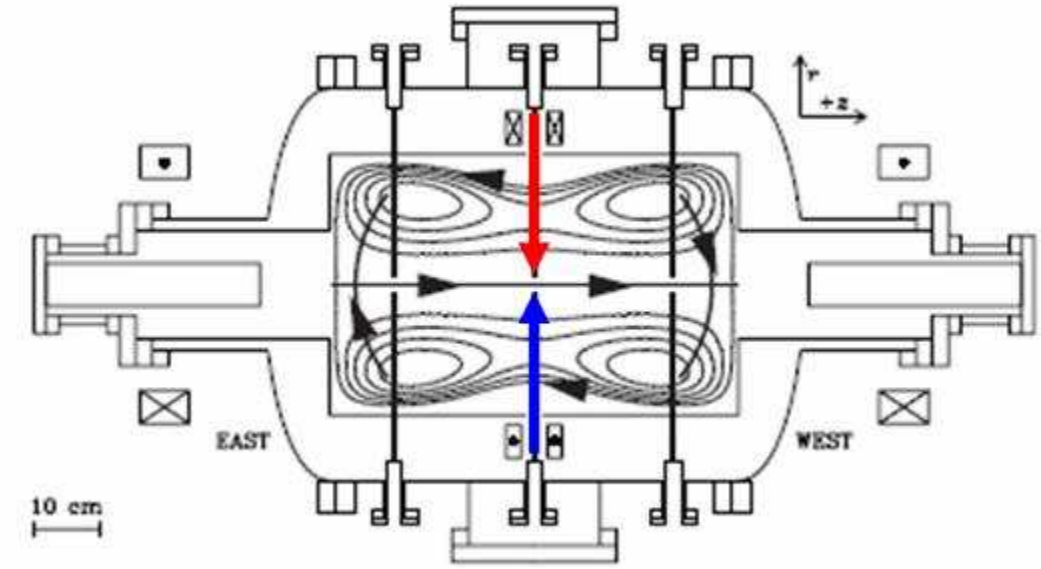

Fig. 5.— Schematic of the SSX setup. A cross-section is shown–the device is cylindrically symmetric about the horizontal axis in the figure. Spheromak plasmas are formed in the guns on the east and west sides of the vacuum chamber and ejected into the main flux conserver. Gaps in the center of the flux conserver allow external, photon-based diagnostics to gather data. The arrows represent the lines of sight of the VUV monochromator (red) and soft x-ray detector (blue). Other diagnostics currently in use in SSX include an ion Doppler spectrometer, a Mach probe to measure flow velocities, a He-Ne quadrature interferometer for measuring density, and an array of magnetic probes (shown as black lines in the figure). The contours drawn inside the flux conserver are the magnetic field lines of an FRC, the plasma structure that forms when two counter-helicity spheromaks merge. Figure modified from (9).

of 0.61 m. There is a 2 cm gap between the two flux conservers at the midplane to allow access to the plasma for experimental diagnostics.

The spheromak formation process is illustrated in Figure 6. The energy for creating the plasma is provided by four 0.5 mF capacitors that can be charged to a maximum voltage of 10 kV. To initiate an SSX shot, hydrogen gas is pumped into the space between the inner and outer gun electrodes. After a short time delay to allow the gas to fill the guns (the standard value for this time delay is 730 μs–decreasing

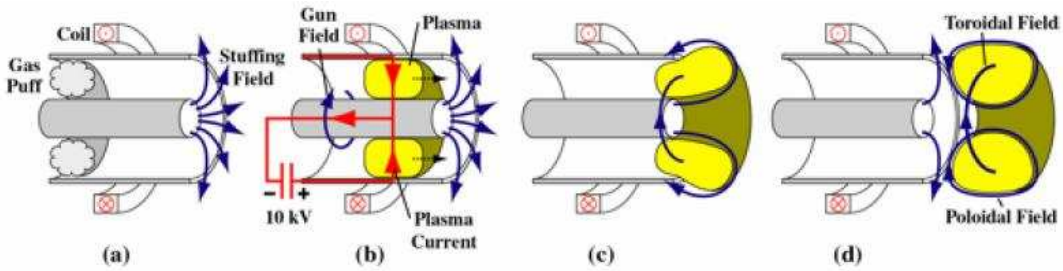

Fig. 6.— Schematic of spheromak formation in SSX. (a) Hydrogen gas is pumped into the space between the inner and outer electrodes, while current through the outer coils creates a "stuffing field." (b) The main capacitor banks discharge, ionizing the gas as a radial current flows from the outer to the inner electrode. (c) The $\mathbf{J} \times \mathbf{B}$ force between the gun field and the plasma current accelerates the spheromak out of the gun. (d) The plasma drags along the stuffing field, which reconnects to form the poloidal field of the spheromak. Figure from (11).

this time leads to the creation of a lower density plasma), the main capacitor banks discharge, creating a high potential difference between the inner and outer gun electrodes. This voltage ionizes the gas in the gun.

As shown in Figure 6b, once the gas becomes partially ionized, the plasma's conductivity allows a current to flow from the positive capacitor plate along the outer electrode, through the plasma, and back along the inner electrode to the negative capacitor plate. The current flowing down the inner electrode creates a magnetic field in the gun that becomes the toroidal field of the spheromak. The interaction of this field with the plasma current through the $\mathbf{J} \times \mathbf{B}$ force accelerates the spheromak out of the gun.

Approximately 25 ms before the main capacitor banks discharge, a seperate set of capacitors discharges and drives current through a coil encircling each gun. This current creates a dipole-like "stuffing field." As the plasma exits the gun, it runs into the stuffing field. As we will see in Chapter 2, to a first approximation, magnetic

field lines are frozen into the plasma, so the stuffing field is dragged along with the spheromak. When the plasma gets far enough out of the gun, the stuffing field breaks off and reconnects to form the poloidal field of the spheromak.

Research at SSX focuses primarily on the merging of two spheromaks in the center of the flux conserver, for it is during this process that large-scale magnetic reconnection occurs. When spheromaks of the same helicity merge, the poloidal fields reconnect and a single, larger spheromak is formed. Counter-helicity mergings, on the other hand, lead to the creation of a new equilibrium state known as a Field Reversed Configuration (FRC) (see Figure 5) (9). During counter-helicity merging, both the toroidal and poloidal fields of the spheromaks reconnect, releasing large amounts of energy in the form of heating and bulk plasma flows. Reconnection results in the annihilation of the toroidal fields, so FRCs have only poloidal fields. The helicity of SSX spheromaks can be easily reversed by changing the direction of current in the stuffing coils, allowing for the study of both co-helicity and counter-helicity merging.

2. Theory

2.1. MHD Theory and Magnetic Reconnection

Deriving a useful theory of plasma behavior poses a unique problem because of the nature of charged particle interactions. Ions and electrons in plasmas generate changing electric and magnetic fields as they move, but at the same time their motions are effected by these very fields. An obvious tactic would be to calculate the trajectory of each particle individually; however, a typical plasma might have a density of 10^{12} or more ion-electron pairs per cm^3 (the SSX plasma density is around 5×10^{14} ions/cm^3), and today's best computer simulations can only follow $\sim 10^9$ particles for a few ns. Fortunately, it turns out that the majority of plasma phenomena can be accurately described by ignoring individual particle motion and applying the tools of fluid mechanics to the study of plasma dynamics. This theory, known as magnetohydrodynamics (MHD), integrates the equations of classical electromagnetism into the standard fluid model in order to describe plasma motion. For certain low density plasmas, ion and electron velocity distributions may not be Maxwellian, and MHD can no longer be applied. A more complex treatment known as plasma kinetic theory has been developed for these instances, but I will focus on MHD and the realms in which it produces accurate results. The following discussion draws from (6), (11), and (9).

2.1.1. The MHD Approximation

MHD allows us to describe the state of a plasma in terms of a few bulk variables: the density n, pressure p, electric and magnetic fields $\mathbf{E}$ and $\mathbf{B}$, current density $\mathbf{J}$, and flow velocity $\mathbf{v}$. Counting each of the vectors as three variables, we see that we

need 14 independent equations to define a fully constrained model. As with many problems in electromagnetics, it makes sense to begin with Maxwell's equations:

$$\nabla \cdot \mathbf{E} = \frac{\rho}{\epsilon_0} \tag{2.1}$$

$$\nabla \times \mathbf{E} = -\frac{\partial \mathbf{B}}{\partial t} \tag{2.2}$$

$$\nabla \cdot \mathbf{B} = 0 \tag{2.3}$$

$$\nabla \times \mathbf{B} = \mu_0(\mathbf{J} + \epsilon_\mathbf{0}\frac{\partial \mathbf{E}}{\partial \mathbf{t}}) \tag{2.4}$$

The charge density ρ is 0 on large scales in plasmas due to Debye shielding; however, the divergence of the electric field at any one point is not necessarily 0. This is the essence of the dilemma that we face when attempting to construct an approximate theory of plasma dynamics. Fortunately, it turns out that we can discard Gauss's law (equation 2.1) and still derive a complete set of equations. Furthermore, if take the divergence of Faraday's law (equation 2.2), we get

$$\nabla \cdot \nabla \times \mathbf{E} = -\nabla \cdot \frac{\partial \mathbf{B}}{\partial t} \tag{2.5}$$

$$0 = \frac{\partial}{\partial t}(\nabla \cdot \mathbf{B}) \tag{2.6}$$

which implies that $\nabla \cdot \mathbf{B}$ is constant in time, so equation 2.3 is actually an initial condition rather than an independent equation.

We can derive several more equations by considering the plasma's fluid properties. Neglecting the effects of ionization and recombination, the total number of particles N in a volume V of plasma can only change if there is a net flux of particles across the surface S bounding that volume. Therefore, by the divergence theorem

$$\frac{\partial N}{\partial t} = \int_V \frac{\partial n}{\partial t} dV = -\oint_S n\mathbf{v} \cdot d\mathbf{S} = -\int_V \nabla \cdot (n\mathbf{v}) dV \tag{2.7}$$

This must hold for any volume V, so the integrands of the volume integrals must be equal, and we have the equation of continuity

$$\frac{\partial N}{\partial t} + \nabla \cdot (n\mathbf{v}) = \mathbf{0} \tag{2.8}$$

The density n can be related to the pressure p by the thermodynamic equation of state of the plasma, which takes the form

$$p = Cn^{\gamma} \tag{2.9}$$

where γ is the ratio of the specific heat at constant pressure to the specific heat at constant volume and C is a constant. For isothermal compression or expansion, $\gamma = 1$, while for adiabatic compression or expansion with three degrees of freedom, $\gamma = 5/3$.

No set of governing equations for a system would be complete without Newton's second law. We begin by considering the forces on electrons and ions in the plasma separately. Neglecting gravity, an electron in an ionized plasma can feel a force from pressure gradients, electric fields, and magnetic fields (Lorentz force). Then in terms of the electron mass m_e, density n_e, velocity v_e, and pressure p_e

$$m_e n_e \frac{d\mathbf{v_e}}{dt} = -en_e(\mathbf{E} + \mathbf{v_e} \times \mathbf{B}) - \nabla p_e \tag{2.10}$$

The derivative on the left hand side of this equation describes the acceleration of electrons in their own frame; it would be more convenient to have an equation that applies for fluid elements that are fixed in space. In one dimension, the change in an arbitrary fluid property $\mathbf{K}$ in a frame moving with the fluid can be written as the sum of two terms

$$\frac{d\mathbf{K}(x,t)}{dt} = \frac{\partial \mathbf{K}}{\partial t} + \frac{\partial \mathbf{K}}{\partial x}\frac{dx}{dt} = \frac{\partial \mathbf{K}}{\partial t} + u_x \frac{\partial \mathbf{K}}{\partial x} \tag{2.11}$$

This generalizes in three dimensions to

$$\frac{d\mathbf{K}}{dt} = \frac{\partial \mathbf{K}}{\partial t} + (\mathbf{v} \cdot \nabla)\mathbf{K} \tag{2.12}$$

This is known as a convective derivative. To understand its meaning intuitively, consider a pot of water on a stove. The temperature at a fixed location in the water

can change because heat is transferred to the water from the stove element, warming the water everywhere in the pot (the partial derivative term), or because hot water moves into the location of interest and displaces the cooler water that was already there (the convective term). Inserting the convective derivative into the electron equation of motion, we have

$$m_e n_e \left[\frac{\partial \mathbf{v_e}}{\partial t} + (\mathbf{v_e} \cdot \nabla)\mathbf{v_e}\right] = -en_e(\mathbf{E} + \mathbf{v_e} \times \mathbf{B}) - \nabla p_e \tag{2.13}$$

An analogous equation can be written for the ions in the plasma

$$m_i n_i \left[\frac{\partial \mathbf{v_i}}{\partial t} + (\mathbf{v_i} \cdot \nabla)\mathbf{v_i}\right] = en_i(\mathbf{E} + \mathbf{v_i} \times \mathbf{B}) - \nabla p_i \tag{2.14}$$

Assuming $n_e = n_i$, we can add equation 2.13 and 2.14 to get

$$\rho \left[\frac{\partial \mathbf{v}}{\partial t} + (\mathbf{v} \cdot \nabla)\mathbf{v}\right] = \mathbf{J} \times \mathbf{B} - \nabla \mathbf{p} \tag{2.15}$$

because $en(\mathbf{v_i} - \mathbf{v_e}) = \mathbf{J}$. A more complete derivation would allow for the possibility of shearing (for example, motion in the x-direction leading to momentum transfer in the y-direction) by replacing ∇p by the divergence of the pressure tensor $\mathbf{P}$.

The final three necessary equations come from Ohm's law, which describes the electrical properties of the plasma. In its most generalized form, Ohm's law is rather daunting, but we can often neglect several terms and write

$$\mathbf{E} + \mathbf{v} \times \mathbf{B} = \eta \mathbf{J} \tag{2.16}$$

where the terms on the left represent the electrostatic force and the Lorentz force, and η is the plasma resistivity. In *ideal MHD*, we make one more approximation and assume that the plasma is perfectly conducting, so

$$\mathbf{E} + \mathbf{v} \times \mathbf{B} = \mathbf{0} \tag{2.17}$$

Equations 2.2, 2.4, 2.8, 2.9, 2.15, and 2.17 turn out to be extremely useful for understanding large scale plasma behavior.

2.1.2. Frozen-in-Flux

An interesting consequence of the ideal MHD assumptions is that magnetic field lines are "frozen" into the plasma, meaning that they move only along with the bulk plasma flow patterns. The frozen-in flux theorem, or Alfvén's theorem, states that the flux through a surface that moves with the plasma is constant in time. To see why, we follow (38) and (11) and substitute Ampere's law (equation 2.4) into the resistive Ohm's law (equation 2.16). The displacement current $\frac{\partial \mathbf{E}}{\partial t}$ can be neglected in MHD because the time scale for diffusion is much longer than the time scale for light to propogate in the plasma (9), so we get

$$\mathbf{E} = -\mathbf{v} \times \mathbf{B} + \frac{\eta}{\mu_0} \nabla \times \mathbf{B} \tag{2.18}$$

assuming that the resistivity is constant throughout the plasma. Taking the curl of both sides

$$\nabla \times \mathbf{E} = -\nabla \times \mathbf{v} \times \mathbf{B} + \nabla \times \frac{\eta}{\mu_0} \nabla \times \mathbf{B} \tag{2.19}$$

Now we can use Faraday's law (equation 2.2) to eliminate $\mathbf{E}$, leaving us with

$$\frac{\partial \mathbf{B}}{\partial t} = \nabla \times \mathbf{v} \times \mathbf{B} + \frac{\eta}{\mu_0} \nabla^2 \mathbf{B} \tag{2.20}$$

This is known as the magnetic induction equation. Recalling the assumptions of ideal MHD, we can set the resistivity equal to zero, so

$$\frac{\partial \mathbf{B}}{\partial t} = \nabla \times \mathbf{v} \times \mathbf{B} \tag{2.21}$$

Now consider a curve C bounding a surface S which is moving through the plasma (see Figure 7). In a time dt an element $d\mathbf{l}$ of C sweeps out an area $d\mathbf{S} = \mathbf{v} \times d\mathbf{l} dt$. Therefore, by the product rule, the rate of change of magnetic flux through C is

$$\frac{d\Phi}{dt} = \frac{d}{dt} \int_S \mathbf{B} \cdot d\mathbf{S} = \int_S \frac{\partial \mathbf{B}}{\partial t} \cdot d\mathbf{S} + \int_C \mathbf{B} \cdot \mathbf{v} \times d\mathbf{l} \tag{2.22}$$

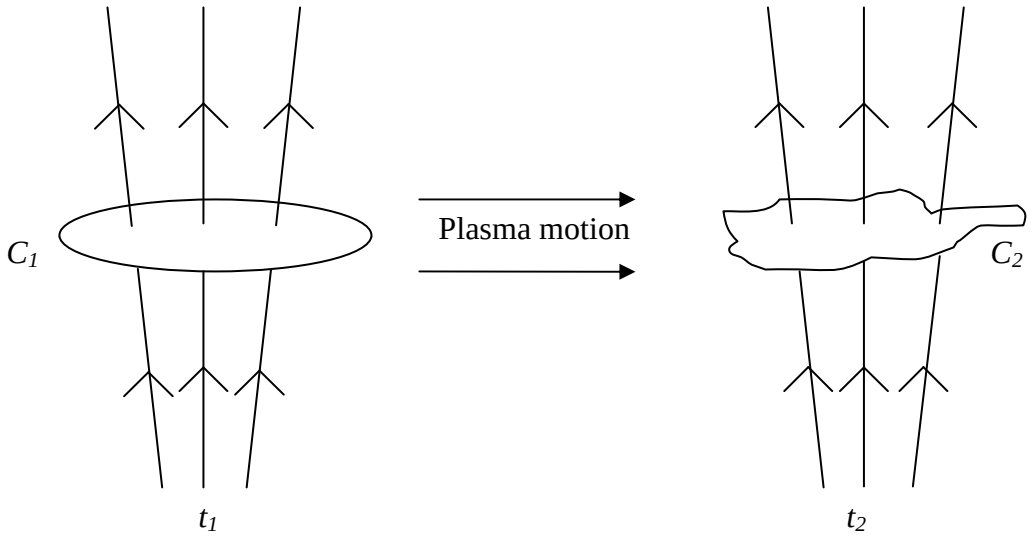

Fig. 7.— Magnetic flux conservation in ideal MHD. If a curve C_1 is distorted into C_2 by plasma motion, then the flux through C_1 at t_1 and the flux through C_2 at t_2 will be equal because magnetic field lines are "frozen-in."

This expression is analogous to the convective derivative described earlier. As C moves, the flux through the loop can change either because the magnetic field is changing in time (the first term on the right) or because the boundary is moving in space (the second term on the right). Using a vector identity, $\mathbf{B} \cdot \mathbf{v} \times d\mathbf{l} = -\mathbf{v} \times \mathbf{B} \cdot d\mathbf{l}$, so

$$\frac{d\Phi}{dt} = \int_S \frac{\partial \mathbf{B}}{\partial t} \cdot d\mathbf{S} - \int_C \mathbf{v} \times \mathbf{B} \cdot d\mathbf{l} \tag{2.23}$$

Finally, applying Stokes' theorem to the second term

$$\frac{d\Phi}{dt} = \int_S \left[\frac{\partial \mathbf{B}}{\partial t} - \nabla \times (\mathbf{v} \times \mathbf{B}) \right] \cdot d\mathbf{S} = 0 \tag{2.24}$$

from equation 2.21. So the flux through C is constant in time.

2.1.3. Resistive MHD

As one might expect, real plasmas are not perfectly conducting, so ideal MHD fails to predict several interesting plasma phenomena. In particular, when real plasma components carrying oppositely directed magnetic fields run into one another, high field gradients can cause field lines to diffuse through the plasma, change their topology, and reconnect, converting stored magnetic energy into kinetic energy or heat. In other words, the frozen-in-flux condition is violated. Studying magnetic reconnection is the primary goal of SSX.

Let us return to the induction equation (2.20), this time allowing the plasma resistivity to be non-zero.

$$\frac{\partial \mathbf{B}}{\partial t} = \nabla \times \mathbf{v} \times \mathbf{B} + \frac{\eta}{\mu_0} \nabla^2 \mathbf{B} \tag{2.25}$$

If we consider only the first term on the right hand side, we get equation 2.21, which describes changes in the magnetic field brought about by convective motions of plasma with frozen-in flux. Considering only the second term, the equation becomes

$$\frac{\partial \mathbf{B}}{\partial t} = \frac{\eta}{\mu_0} \nabla^2 \mathbf{B} \tag{2.26}$$

This has the standard form of a diffusion equation, so we see that in resistive MHD, magnetic fields can change through diffusion as well as convection.

We can characterize the importance of convection versus diffusion in a particular plasma by taking the ratio of the two components of the induction equation. If L is the characteristic length scale in the plasma, the spatial derivative ∇ can be approximated by $\frac{1}{L}$. Then

$$\frac{convection}{diffusion} \approx \frac{(1/L)vB}{\eta B/\mu_0 L^2} = \frac{\mu_0 L v}{\eta} \equiv R_M \tag{2.27}$$

The quantity R_M is known as the magnetic Reynolds number.

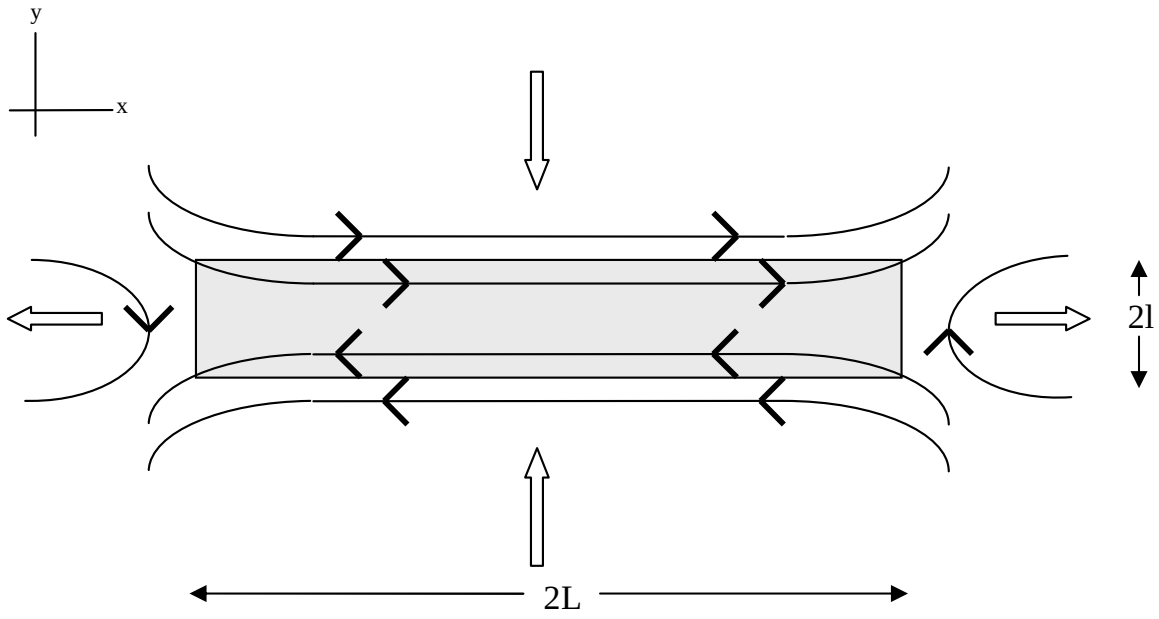

Fig. 8.— Sweet-Parker reconnection model geometry. The hollow arrows represent the direction of plasma flow, while the smaller black arrows show the direction of the embedded magnetic fields. Reconnection occurs within the shaded region.

2.1.4. Sweet-Parker Magnetic Reconnection

Now that we have relaxed our assumptions so that magnetic field lines may diffuse through the plasma and reconnect, we would like to have a model for the nature of this process and the rate at which it will occur. The first and simplest model of magnetic reconnection was proposed by Sweet and Parker (33) in the late 1950s. The following discussion draws from (4), (38), and (11).

The Sweet-Parker model assumes that reconnection occurs entirely in two dimensions. Field lines are assumed to be approximately straight, but with just enough curvature that we can define a rectangular reconnection region of length 2L and thickness 2l (see Figure 8). Plasma components containing opposing magnetic fields flow in from the $\pm y$ directions with velocity v_{in}. Inside the reconnection region, magnetic field gradients become high enough that field lines that were previously frozen in can

diffuse and reconnect; after reconnection field lines and plasma flow out in the $\pm x$ directions with velocity v_{out}. The model assumes that reconnection is a steady-state process, so v_{in} and v_{out} do not change with time. In other words, although plasma is constantly moving and individual field lines are changing their topology, if we took a snapshot of the reconnection region at any time, it would always look the same. With this in mind, we can see that mass continuity implies

$$4\rho L v_{in} = 4\rho l v_{out} \tag{2.28}$$

$$L v_{in} = l v_{out} \tag{2.29}$$

if we assume that the plasma is incompressible.

Outside the reconnection region, the magnetic field lines are approximately straight, so $\nabla \times \mathbf{B} = 0$ and Ampere's law (equation 2.4) tells us that there is no current. The z-component of the resistive Ohm's law (equation 2.16) then becomes

$$E_z + v_{in} B_{in} = 0 \tag{2.30}$$

Inside the region, the net magnetic field is zero, so the z-component of Ohm's law gives

$$E_z = \eta J_z \tag{2.31}$$

We can combine these two relations by noting that the steady-state assumption implies $\frac{d\mathbf{B}}{dt} = 0$, so by Faraday's law (equation 2.2), $\nabla \times E = 0$ and the electric fields inside and outside the region are the same. So we have

$$v_{in} B_{in} = \eta J_z \tag{2.32}$$

Now we may apply Ampere's law to the reconnection region as a whole. Equating the line integral of $\mathbf{B}$ around the border of the region to the enclosed current density,

we find

$$B_{in}(4L) = \mu_0 J_z(2L)(2l) \tag{2.33}$$

$$B_{in} = \mu_0 J_z l \tag{2.34}$$

Substituting this expression into our result from Ohm's law

$$v_{in} = \frac{\eta}{\mu_0 l} \tag{2.35}$$

$$\frac{v_{in}\mu_0 l}{\eta} = R_m = 1 \tag{2.36}$$

So the magnetic Reynolds number is 1 during Sweet-Parker reconnection, implying that the inflow velocity and thickness of the reconnection region adjust themselves until magnetic flux is being annihilated at the same rate that plasma is escaping out the sides of the region.

During reconnection, magnetic energy stored in the incoming field is converted into kinetic energy of the outgoing plasma, so we can conserve energy to find the outflow velocity in the ideal case with no plasma heating.

$$\frac{B_{in}^2}{2\mu_0} = \frac{\rho v_{out}^2}{2} \tag{2.37}$$

$$v_{out} = \frac{B_{in}}{\sqrt{\mu_0 \rho}} \tag{2.38}$$

This velocity represents a sort of speed limit in the plasma; it is known as the Alfvén speed (v_A). v_A has additional importance in MHD theory as the phase velocity of large-scale, low-frequency oscillations known as Alfvén waves.

Now we can combine equations to relate v_{in} and v_{out}

$$v_{in}^2 = (v_{in})(v_{in}) = (\frac{v_{out} l}{L})(\frac{\eta}{\mu_0 l}) = v_{out}^2(\frac{\eta}{v_{out}\mu_0 L}) \tag{2.39}$$

The reconnection rate (M) is often expressed in terms of the Alfvén speed in order to allow for straightforward comparisons between plasmas. Recalling that $v_{out} = v_A$,

we have

$$M \equiv \frac{v_{in}}{v_A} \tag{2.40}$$

$$M = \sqrt{\frac{v_A \mu_0 L}{\eta}} = \frac{1}{\sqrt{S}} \tag{2.41}$$

where S is a special case of the Reynold's number (known as the Lundquist number) that represents how well magnetic field lines are frozen to the plasma. Experimental results show that the $\frac{1}{\sqrt{S}}$ reconnection rate predicted by Sweet-Parker is too slow, and more sophisticated models of reconnection have since been developed. Furthermore, results at SSX (5) and elsewhere have shown that the interactions between reconnection fields are not confined to a planar interface. However, Sweet-Parker remains a useful introduction to the theory of reconnection, and the two-dimensional model provides an ideal framework for understanding the basic processes at work.

2.2. Excitation kinematics

As discussed earlier, external, photon-based diagnostics play an important role in the analysis of laboratory plasma properties. To understand the meaning of measurements made by such diagnostics, we must move beyond the large-scale descriptions provided by MHD theory and focus on the processes at the atomic level that cause plasmas to radiate. The following discussion draws from (39), (29), and (9).

2.2.1. Sources of emission

For plasmas that are optically thin (meaning that the typical photon produced in the plasma escapes without being absorbed or scattered), the most important radiative processes are line emission, radiative recombination, and bremsstrahlung

radiation. The SSX plasma is optically thin at most photon energies, although it may become optically thick at the wavelength of some resonant atomic transitions.

Bremsstrahlung radiation ("braking radiation") originates from the acceleration of a charged particle due to the electric field of another particle. The total power radiated by a system of accelerating charges can be approximated by

$$P = \frac{2\ddot{\mathbf{d}}^2}{3c^3} \tag{2.42}$$

where $\mathbf{d}$ is the electric dipole moment of the system, defined by

$$\mathbf{d} = \sum_i q_i \mathbf{r}_i \tag{2.43}$$

Collisions between two identical particles create no net acceleration of the system's dipole moment, so the total radiated power vanishes in the dipole limit and can usually be neglected. Therefore, the main contributer to bremsstrahlung radiation in plasmas is electron-ion collions. In practice, the radiation is dominated by the acceleration of electrons; the large mass discrepency between electrons and ions means that the change in the ion's velocity during an electron-ion collision is negligible. Bremsstralung radiation is also known as "free-free" emission because it is caused by electron transitions between two unbound, or "free", states of the target ion.

The spectral signature of bremsstralung radiation is a smooth continuum, since electron and ion velocities in a plamsa are continuously distributed. The total free-free emission at a given energy can be obtained by integrating over the electron velocity distribution, all possible impact parameters, and the particle distribution in the plasma. Assuming a Maxwellian electron velocity distribution, the emissivity is

$$\epsilon = \frac{2^5 \pi e^6}{3 m_e c^3} \sqrt{\frac{2\pi}{e m_e k T}} Z^2 n_e n_i e^{-h\nu/kT} g_{ff} \tag{2.44}$$

where Z is the atomic number of the colliding ions, h is Planck's constant, and g_{ff} is a quantum mechanical correction known as the *Gaunt factor*. The dimensions of

the emissivity are power/unit volume/unit energy range, or in the units that will be used later on, erg/s/cm^3/eV.

The SSX plasma is made of hydrogen, nearly 100% of which is ionized. However, even in an equilibrium state of nearly complete ionization, electrons are constantly recombining with protons before being knocked loose again by collisions. Energy is conserved in this process through the emission of a photon of energy

$$E = \frac{13.6 \text{ eV}}{n^2} + K \tag{2.45}$$

where n is the hydrogen energy level into which the electron recombines and K is the initial kinetic energy of the electron. Since n can range from 1 to ∞, and the range of possible electron kinetic energies is continuous, radiative recombination is a continuum process. Electrons with velocities at the low end of the distribution are the most likely to combine, so the majority of photons emitted as a result of recombinations into an energy level n will have energies close to 13.6 eV/n^2. As we shall see in Chapter 4, radiative recombination is in fact a far greater contributor to the emission spectrum in SSX than is bremsstrahlung radiation.

For the conditions present in SSX, the dominant spectral features come not from continuum processes at all but from line radiation produced by transitions of electrons bound to ions. When an electron residing in an excited state of an atom falls back to a lower state, a photon with energy equal to the difference in energy between the two atomic levels is spontaneously emitted.

Given that SSX features a highly ionized hydrogen plasma, one might think that the contribution of line radiation to the observed spectrum would be negligible. However, if the hydrogen atoms formed as a result of recombinations into excited states are not immediately re-ionized, additional photons will be emitted as the electrons cascade down to the ground state. More importantly, despite the best efforts of exper-

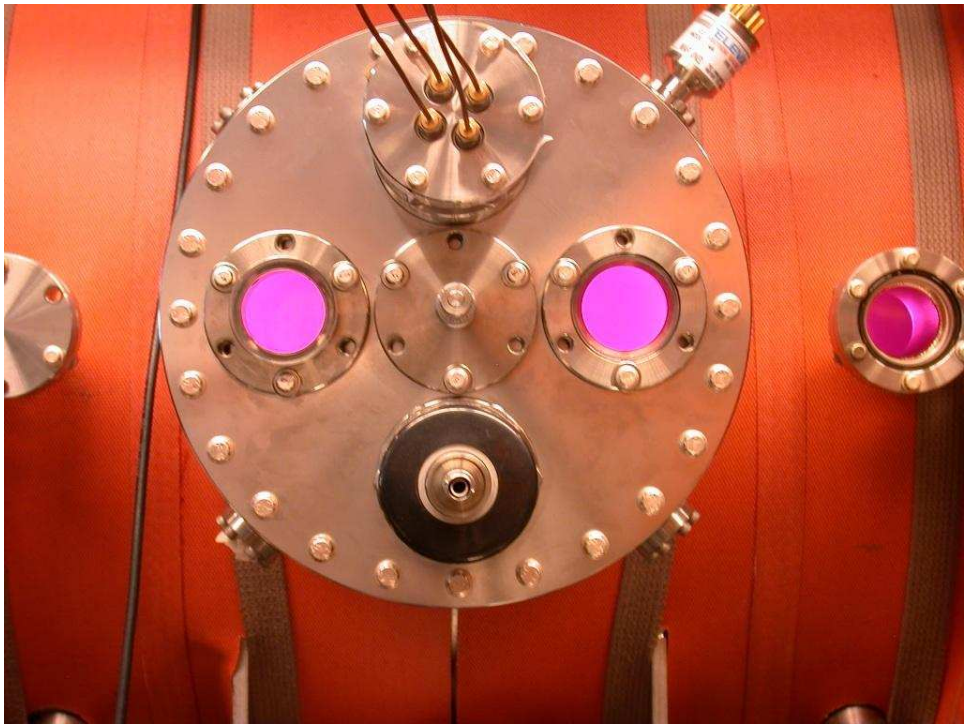

Fig. 9.— Photo taken during an SSX shot. Visible emission from the plasma can be seen through the three windows into the flux conserver. The light appears purple because of emission from Balmer series hydrogen lines that appear during recombination of protons and electrons.

imentalists, all laboratory plasmas contain impurities. While detrimental to plasma performance, these impurities are a blessing in disguise, because observing line emission from impurity ions is one of the best diagnostic tools that plasma physicists have. Observations have shown that the dominant impurity in SSX is carbon, comprising perhaps as much as one percent or more of the plasma material (26). Other impurities present in smaller quantities include oxygen, nitrogen, and possibly metals such as copper. Appendix A contains energy level diagrams for impurity ions present in SSX.

The volume emissivity P_{ji} (photons/cm^3/s) of a particular emission line transition from level j to i is given by

$$P_{ji} = N_j A_{ji} \tag{2.46}$$

where N_j is the population density in cm^{-3} of ions with electrons in the upper line level j and A_{ji} is the probability in s^{-1} of a transition to the lower level i through spontaneous emission of a photon. The level population densities in a plasma can be found by solving a set of rate equations of the form

$$\frac{dN_j}{dt} = \sum_{h<j} N_h n_e S_{hj} \quad + \quad \sum_{k>j} N_k (A_{kj} + n_e S^1_{kj}) + N_{z+1} n_e \alpha^r_j + N_{z-1} n_e \beta^{II}_j$$
$$- \quad N_j \left[\sum_{h<j} (A_{jh} + n_e S^1_{jh}) + \sum_{k>j} n_e S_{jk} + n_e S^i_j \right] \qquad (2.47)$$

In this rather intimidating equation, S_{hj} is the rate coefficient for electron impact ionization from level h to level j, S^1_{kj} is the rate coefficient for collisional de-excitation, N_z represents the population density of ions of charge z, and α^r_j and β^{II}_j are the rate coefficients for recombination and collisional inner-shell ionization, respectively. If we assume a steady-state ($dN_j/dt = 0$), equation 2.47 reduces to a set of linear algebraic equations that can be solved for the level populations. The steady-state assumption is often accurate even in a changing plasma, because excited level populations usually come into equilibrium extremely quickly.

2.2.2. Coronal Equilibrium vs LTE

Equations 2.47 are a complex mess of variables and subscripts which require knowledge of a large number of atomic parameters to solve. Fortunately, at relatively low densities, we can often simplify things by assuming that the plasma is in *coronal equilibrium*. This model, which acquired its name because it was first applied to the solar corona, assumes that all upward atomic transitions are caused by collisions between electrons and ions, and all downward transitions occur through spontaneous emission. If we assume further that excited state lifetimes are low enough that all excitations occur out of the ground state and electron cascades from levels above level

j can be neglected, equation 2.47 reduces to

$$0 = N_g n_e S_{gj} - N_j \sum_{h<j} A_{jh} \tag{2.48}$$

where N_g is the population density of the ground state. This equation is a suitable approximation for many coronal plasmas, but it can be rendered inaccurate by the presence of metastable atomic states or by high enough densities.

As plasma density increases and collisions between electrons and ions become more frequent, the coronal equilibrium model begins to break down. Collisions can excite or ionize electrons out of excited states, and collisional de-excitation (in which the excess energy from an atomic transition is converted into kinetic energy of the colliding electron) also becomes important. At very high densities, the state of the plasma is described by *Local Thermodynamic Equilibrium (LTE)*, a state in which every atomic process is as frequent as its inverse process. For example, collisional excitation and de-excitation are inverse processes, as are spontaneous emission and photoexcitation. This condition is known as the *Principle of Detailed Balancing (PDB)*. At intermediate densities, plasma conditions lie somewhere between the simplified coronal and LTE states, and emission line strengths must be calculated by solving the full rate equations for the atomic level populations and ionization balances.

2.2.3. Calculating Electron Temperature from Line Ratios

Measurements of impurity emission line spectra yield a wealth of information about plasma properties such as temperature, density, composition, and flow velocities. One parameter of particular interest in SSX is the electron temperature T_e. A useful diagnostic of electron temperature is the line intensity ratio of two lines from different ions of the same element. Combining equations 2.46 and 2.48, we see that

emissivity and temperature are related by

$$P_{ji} = N_j A_{ji} = N_g n_e S_{gj} B R_{ji} \tag{2.49}$$

where $BR_{ji} = A_{ji} / \sum_{h<J} A_{jh}$ is the radiative branching ratio with respect to all lower levels. Defining $A_z = N_z/N_H$ (the abundance of element Z relative to hydrogen), $\eta_{Z,z} = N_{Z,z}/N_Z \approx N_g/N_Z$ (the fraction of ions from element Z in ionization stage z), and $G_{ji}(T) = \eta_{Z,z}(T) S_{gj}(T)$, this can be rewritten

$$P_{ji} = n_e N_H A_Z B R_{ji} G_{ji}(T) \tag{2.50}$$

The function $G_{ji}(T)$ represents the electron temperature dependence due to the combination of ionization and excitation.

In the coronal approximation, collisional ionization and radiative recombination both scale with the square of the plasma density, so the overall ionization balance is density independent and $G_{ji}(T)$ depends only on T. Therefore it is straightforward to use equation 2.50 to calculate electron temperatures from line ratios. At high densities, however, other atomic processes become important, and P_{ji} no longer depends solely on T. Fortunately, we can often still calculate the plasma temperature by considering the ratio of two lines from the same ionization stage with different temperature dependences. Alternately, if we have accurate measurements of the plasma density, we may be able to derive electron temperatures from line ratios involving two different inoization stages even if the plasma is not in coronal equilibrium.

3. Experimental Diagnostics

The proximity of laboratory plasmas makes them easier to study than astrophysical plasmas, but the high energies, low densities, and short time scales involved still provide a unique set of challenges for experimentalists. One diagnostic approach is to insert probes into the plasma to directly measure quantities such as magnetic field strengths and bulk flow velocities. These internal measurements can provide valuable information about local plasma properties, but they inevitably perturb the plasma in the process. Furthermore, probes can only take data in a small number of regions and therefore risk misrepresenting the large-scale structure in inhomogenous plasmas.

A second approach to studying plasmas takes advantage of the emission spectra produced by impurity ions. As outlined in Chapter 2, the features apparent in these spectra are determined by a number of important plasma propeties such as temperature, density, impurity concentrations, and flow velocities. Unlike internal diagnostics like magnetic probes, spectrometers and other external diagnostics do not alter the plasma properties being measured in any way. However, they can only take data averaged along a line of sight, and even the extraction of volume-averaged plasma properties from spectral data requires significant computational analysis. The computational techniques used in this study will be the subject of Chapter 4.

In practice, research at SSX utilizes both internal and external plasma diagnostics to produce a complete picture of magnetic reconnection dynamics. This thesis focuses on data taken using two diagnostics: a vacuum ultraviolet (VUV) monochromator, and a low-resolution soft x-ray detector (SXR). Both operate outside the main vacuum chamber (see Figure 5), collecting emitted photons with extremely high time-resolution (10 ns for the VUV monochromator and 5 ns for SXR). The primary goal of these measurements is to develop a method for calculating accurate electron tem-

perature profiles for SSX shots. Simultaneous research at SSX focused on internal measurements of magnetic field structures and bulk flows; results of these studies can be found in (17).

3.1. VUV Spectroscopy

The VUV monochromator was used to observe individual emission lines from carbon, oxygen, and nitrogen ions. By comparing average line intensity ratios over a number of shots to theoretical values from computer simulations, we were able to determine typical values for the electron temperature during single-spheromak, co-helicity merging, and counter-helicity merging shots. Information in the following sections was drawn from (26).

3.1.1. The SSX VUV monochromator

The vacuum ultraviolet monochromator used at SSX has a focal length of 0.2 m. Photons enter the device through a slit of adjustable width and strike a reflective diffraction grating, which selects and refocuses a narrow bandwidth around the desired central wavelength. The wavelength-selection dial can be manually adjusted with a precision of about 0.2 nm or fine-tuned mechanically if greater precision is desired. Light from the diffraction grating is redirected through an exit slit and into an 800 V photomultiplier tube (PMT).

Adjusting the width of the exit slit changes the spectral resolution, with a 1 mm exit slit width corresponding to 4 nm in wavelength space. Adjusting the entrance slit width, on the other hand, increases the total number of photons that enter the monochromator. We experimented with various combinations of entrance and exit

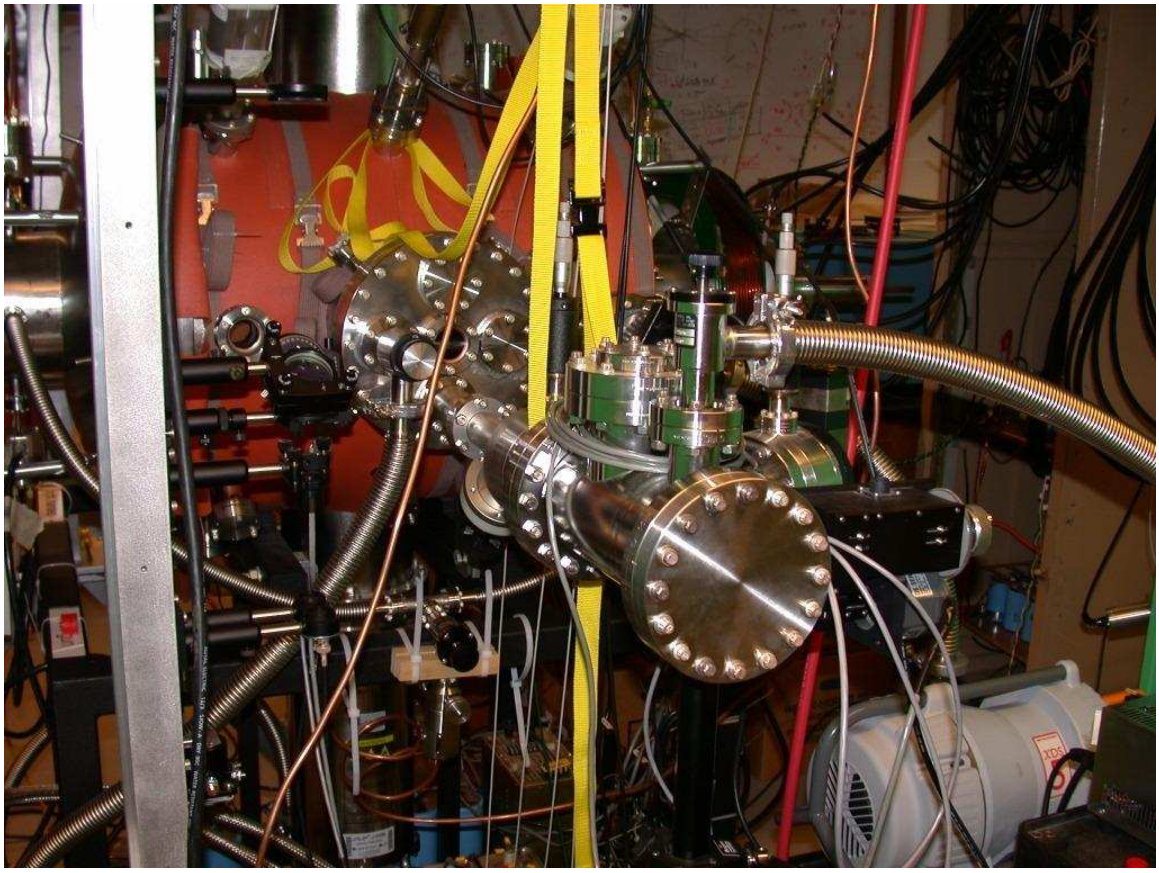

Fig. 10.— Photo of the SSX VUV monochromator. The main vacuum chamber is the orange object in the background.

slit widths and eventually settled on a 1 mm entrance slit width and a 500 μm exit slit width. This exit slit width corresponds to a spectral resolution of 2 nm, which we observed to be ideal for capturing essentially all of the emission from a single broadened impurity line without contaminating the signal with emission from additional lines.

Signals from the PMT pass through a Stanford Research Systems SR570 current amplifier and are registered at 10 ns intervals by an oscilloscope and transferred to a computer using LabView. Electrical feedback between the main capacitor discharge and the amplifier led to a significant background signal. This was measured by taking

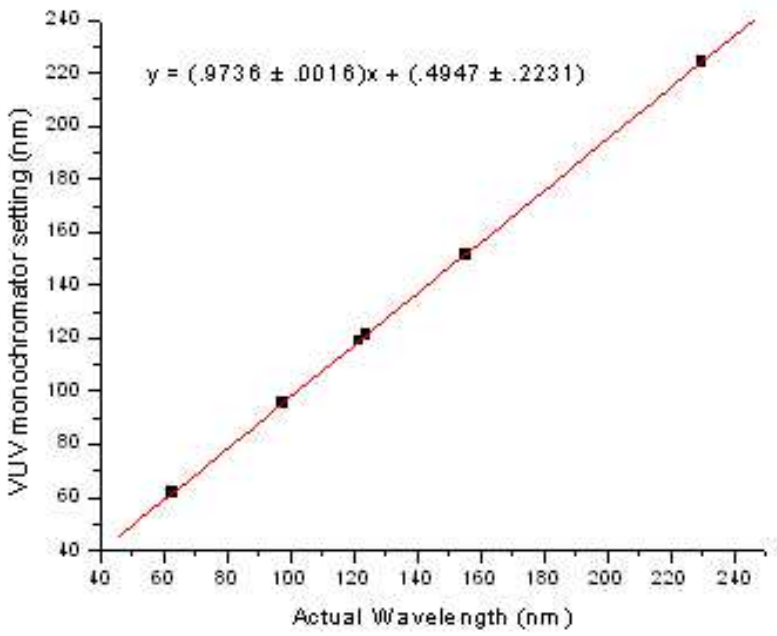

Fig. 11.— VUV monochromator wavelength calibration curve. Data points for the O V 63.0 nm, C III 97.7 nm, H I 121.6 nm, N V 123.9 nm, C IV 155 nm, and C III 229.7 nm lines are shown. The relationship between actual line wavelengths and the monochromator settings necessary to observe them appears to be linear throughout the 50-250 nm wavelength range. The largest deviation from the linear fit occurs for the point at an actual wavelength of 123.9 nm: its predicted VUV monochromator setting (121.1 nm) differs from the optimal setting we found (121.4 nm) by 0.3 nm.

several shots with the monochromator entrance slit closed and then subtracted from the data.

An important practical issue for these experiments is the wavelength calibration of the monochromator. Since the monochromator is used to observe emission lines one at a time, this calibration is vital for the validity of our results. A proper calibration could be achieved by measuring the spectrum of a known plasma source located either in the vacuum chamber or behind a window on the opposite side. However, the quartz windows in SSX only pass photons with wavelengths above 180 nm, so

such a calibration cannot be carried out for much of the wavelength range containing the emission lines of interest (∼50-250 nm). Despite the impossibility of a formal calibration, we were able to construct a useful calibration curve (see Figure 11) by finding the wavelength of peak intensity for a number of impurity lines known to be visible in the SSX plasma (for example, lines that had been observed with ion Doppler spectroscopy).

Absolute intensity calibration of the VUV monochromator also poses a problem, as excessive costs prohibit the use of any accurate calibration methods. Since our results depend on line strength ratios, the intensity calibration is only an issue if it is wavelength-dependent. However, this is certainly a possibility, and we must keep in mind that the lack of an intensity calibration provides an additional source of uncertainty in our measurements of electron temperature.

3.1.2. Previous Observations of VUV lines

Calculations of electron temperature and density in SSX were first carried out by V. S. Lukin and M. R. Brown (26) in 1999-2000. Time-resolved observations were made of four carbon lines: C III 97.7 nm, C III 124.7 nm, C III 229.7 nm, and C IV 155 nm [actually a doublet]. Two peaks were generally observed in the line intensities; one at $t \approx 33$ μs (35 μs for the C IV line) and one at $t \approx 49\,\mu$s. The delay in the timing of the first peak of the CIV line served as evidence that the lines were correctly identified, since it takes longer to strip an atom of three electrons and produce C IV than it does to strip off two electrons and make C III.

A 0-D time-dependent coronal equilibrium simulation code was used to aid in analysis of the data. "0-D" means that the code assumed an isotropic plasma–no variation in plasma parameters was allowed in any direction. Line intensities ratios for

a variety of combinations of electron temperature and density were calculated using the model and compared to experimentally measured ratios in order to determine best-fit values for T_e and n_e. Modeling techniques and their relevance to current work at SSX will be discussed further in Chapter 4.

According to analysis by Lukin and Brown ,the appearance of two distinct peaks in C III line emission was likely explained by the evolution of the plasma temperature during a typical shot. The first peak appeared and then decayed as the plasma "burned through" the C III ionization level (stripping more electrons off the atoms), while the second peak appeared as the plasma began to cool down and electrons and atoms recombined. The decay of the first peak of the C IV line, on the other hand, was probably due to the hottest part of the plasma leaving the line of sight of the monochromator.

Comparison of experimental and simulation results made it possible to constrain the possible values of the SSX electron temperature and density to an almost linear relationship in parameter space. However, conclusive results for the electron temperature profile were not achieved. Simulation results suggested a 229.7 nm / 97.7 nm line ratio of approximately 1/40 for all plausible electron densities, but the experimental data suggested a ratio closer to 1/4.

3.2. Soft X-Ray Detection

Measurements of UV line strength ratios were complemented by data taken using a soft x-ray detector (SXR) composed of photodiodes filtered by thin films of aluminum (Al), Titanium (Ti), Tin (Sn), and Zirconium (Zr). "Soft x-ray" refers to extreme ultraviolet light; SXR is designed to detect photons with energies between 10 and 150 eV. Each SXR filter has a different response function in this energy range

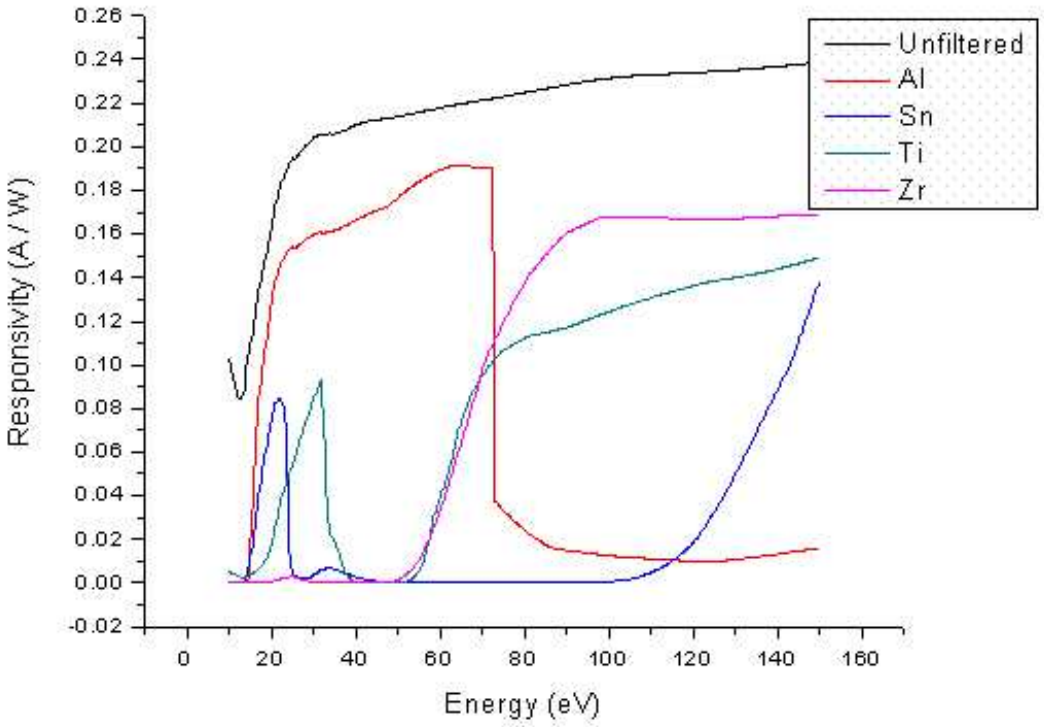

Fig. 12.— SXR filter responsivities. The colored lines show the response function of the filtered diodes in the 10 eV to 150 eV range, and the black line shows the response function of the unfiltered diode.

(see Figure 12), so the ratios of signal strengths registered by each photodiode can yield information about the overall properties of the emission spectrum.

A significant advantage of SXR over the VUV monochromator is that the flux through all four filters can be measured simultaneously. Therefore, we can use SXR data to calculate an electron temperature profile for a particular shot, rather than having to average over many experimental runs. The obvious disadvantage of the device is its low spectral resolution–with only four filters, we cannot obtain information about individual emission lines. However, installing a true x-ray spectrometer is not an option at SSX due to prohibitive costs, so we must settle for a relatively simple

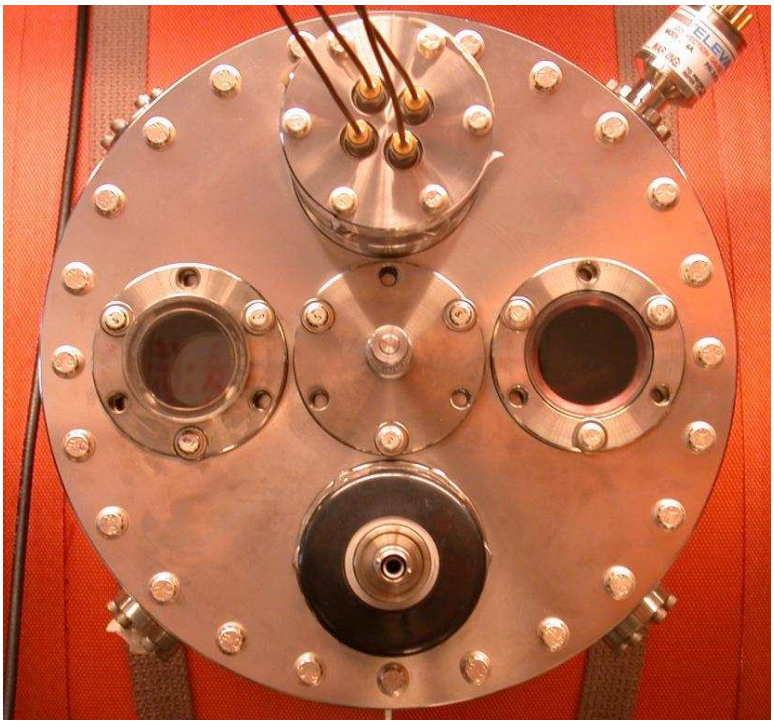

Fig. 13.— Location of SXR on the SSX machine. The four wires at the top of the image carry current from the SXR photodiodes. Clockwise from upper left, the diodes are filtered by foils made of Al, Zr, Sn, and Ti. The VUV monochromator views the plasma from the opposite side of the main vacuum chamber.

picture of the high-energy emission spectrum. Fortunately, we can still determine plasma properties such as the electron temperature with the aid of computer models (see Chapter 4), although the calculations are necessarily more complex (and potentially less accurate) than those used to interpret monochromator data. Our hope is obtain independent measurements of T_e with the VUV monochromator and SXR that can then be compared for corroboration. The following sections draw from (9).

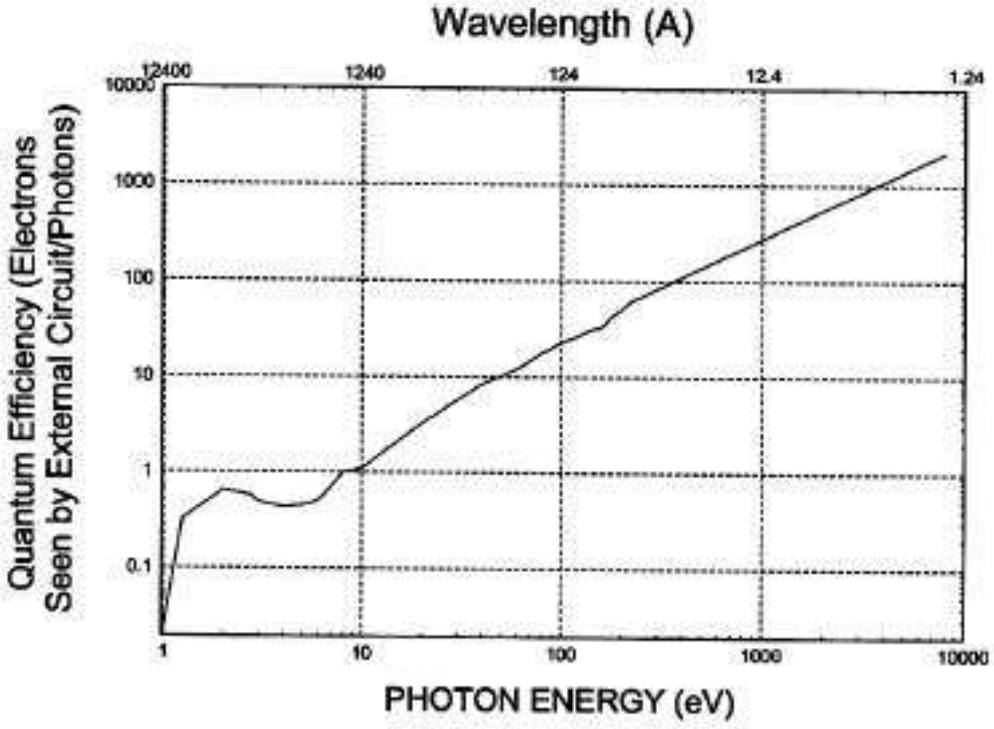

Fig. 14.— Quantum efficiency of the AXUV photodiodes. In the soft x-ray portion of the spectrum (10 eV $<$ E $<$ 150 eV), the quantum efficiency is highly linear, with $Electrons \approx E_{photon}/3.63$. Figure taken from IRD literature.

3.2.1. Design of SXR

The basic concept for SXR has been implemented successfully at several other plasma devices (for example, at the CDX-U spherical torus at Princeton Plasma Physics Laboratory (40) and the Madison symmetric torus reversed-field pinch (15)). Photons enter the detector and strike one of the four filtered photodiodes; those that pass through the filters strike the diode and cause electrons to be released, producing a photocurrent. This current goes into an electrically isolated screen room, where it measured by an oscilloscope.

The SXR uses International Radiation Detectors' (IRD) AXUV silicon p-n junction photodiodes. The model currently in use is the AXUV-HS5, which has a collection area of 1 mm^2 and a rise time of 700 ps when fully biased at 50 V. The photodiodes need not be biased to function properly, however, and at SSX we can achieve the desired time resolution (better than 1 μs) without bias tees in place. When photons of energy 1.12 eV or greater strike the photodiodes, electron-hole pairs are created. The number of carriers produced per photon increases approximately linearly as photon energy increases. In other words, the *quantum efficiency* of the diodes is linear (see Figure 14).

In order to capture the desired information about the soft x-ray portion of the plasma emission spectrum, the photodiodes are filtered by thin metal foils of Al (100 nm thick), Zr (100 nm thick), Sn (100 nm thick), and Ti (50 nm thick). Filter response functions were calculated for a number of possible materials using a calculator provided by the Lawrence Berkeley Laboratory (10). The four foils chosen have response functions that overlap as little as possible, therefore optimizing the spectral resolution that can be achieved with such as small number of filters (see Figure 12) (41). The filters screw onto the photodiodes and can be exchanged or replaced as needed.

Previous experiments with SXR used an array of Neodymium-Iron-Boron magnets to filter out charged particles and make sure only photons struck the photodiodes. While desirable for achieving uncontaminated signals, this approach led to technical difficulties, as the magnets crumbled over time (possibly due to helium embrittlement sustained during glow-discharge cleaning of the vacuum chamber) and blocked the passageways for photons to reach the detector. As a result, the charged particle filter has been abandoned. Comparisons of results with and without the filter suggest that the photocurrents produced by charged particles are minimal. However, we must

keep in mind this additional source of uncertainty as we analyze our measurements.

3.2.2. Previous Work Using SXR

SXR was designed and built in 2002 by A. Falk, M. R. Brown, and C. D. Cothran (9). Initial studies used an indium (In) filter instead of the tin (Sn) filter currently in use. The primary goal was to determine the plasma electron temperature from SXR filter signal ratios. Prior to taking data, a camera flash test was used to ensure that the filters were not passing significant amounts of visible light. The Al, In, and Zr-filtered diodes all generated a current at least three orders of magnitude weaker than the current from the unfiltered diode, but the current produced by the Ti-filtered diode was only two orders of magnitude less than the unfiltered current (see Figure 15). This last result was mildly troubling, but the higher visible transmission of the Ti filter may have been simply an artifact of its thinness (50 nm versus 100 nm for the other three filters).

The currents from all four diodes generally showed three main peaks, at approximately 38 μs, 53 μs, and 65 μs. Signal intensities were seen to increase over a number of shots after the vacuum chamber was vented and re-sealed, implying that the high concentration of impurities in a "dirty" plasma inhibits heating and activity in the plasma. The interpretation of SXR data was aided by comparisons with data from magnetic probes. The first peak was found to correspond to the time when poloidal magnetic reconnection peaked, while the second peak occured as the FRC tilted from the m=0 mode to the lower energy m=1 mode. The cause of the third peak remained a mystery.

The commercial software package Spect3D, by Prism Computational Sciences, Inc. (37), was used to produce model spectra for a variety of plasma sizes, temper-

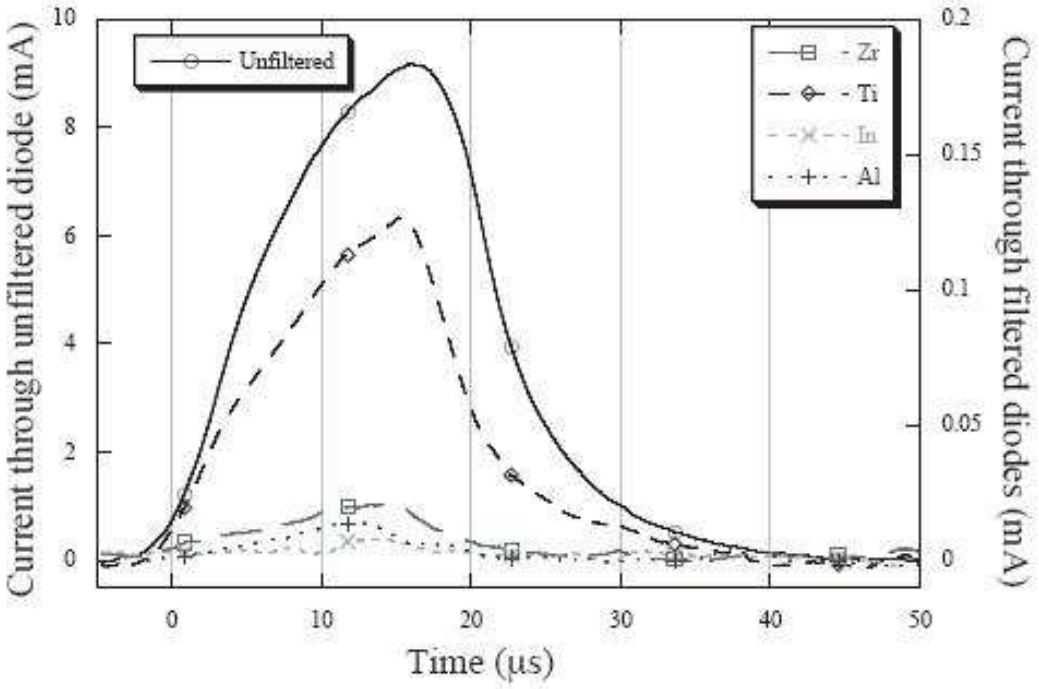

Fig. 15.— SXR Flash Test Results (9). Note that the units on the y-axis are different for the filtered and unfiltered diodes.

atures, densities, and impurity concentrations. Models assumed a spatially uniform plasma in which the coronal approximation was valid. Before the experimental data was fit to the models, the measured SXR signals were divided by the time-dependent density of the plasma squared, as measured by the He-Ne interferometer installed at SSX. This removed the effect of variations in density, since the intensities of both the bremsstrahlung continuum and individual emission lines depend on n^2. Model spectra were smoothed using Spect3D, and the filter signals that each model would have produced were calculated. Model filter ratios were fit to experimental data to determine the best-fit electron temperature as a function of time.

Temperature fits were calculated using four categories of model spectra as hypotheses: bremsstrahlung radiation only, recombination lines and continuum plus

bremsstrahlung but no impurities, 0.5% C and O impurities, and 2.0% C and O impurities. Using the pure bremsstrahlung model, it was determined that counter-helicity merging shots had higher temperatures than co-helicity shots because of greater magnetic reconnection and also had longer liftimes, presumably because FRCs are more stable than spheromaks. Temperature fits using models with impurities were less successful, as the best-fit temperature profiles showed a strong dependence on the precise impurity concentrations used.

Taken as a whole, the calculations by Falk et al. suggested a mean electron temperature in SSX of 30 ± 10 eV. However, the problem of determining T_e turned out to be surprisingly complex, and more work is needed. Models in which only bremsstrahlung radiation is included are obviously not realistic for SSX, since saw in Chapter 2 that the discrete line spectrum of a plasma dominates the continuum at $T < 500$ eV. The continuation of electron temperature studies through advances in modeling techniques and analysis of new data are the subject of this thesis.

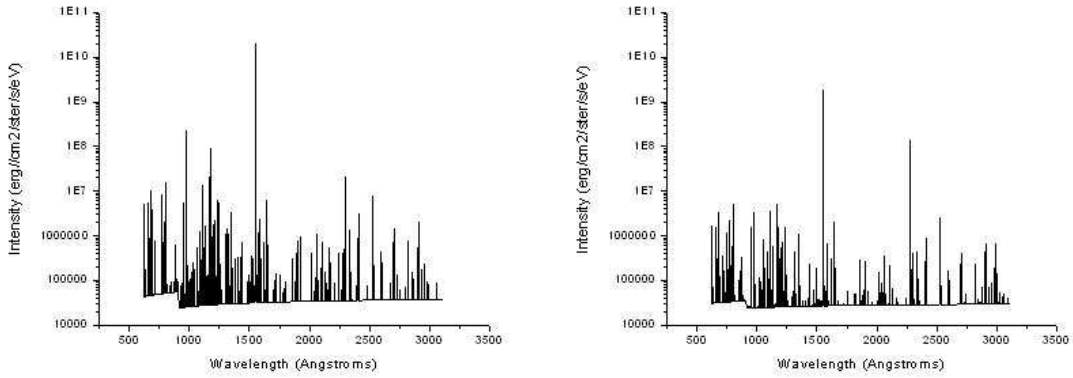

Fig. 16.— Sample PrismSPECT spectra. Both spectra were produced by a 40 cm thick plasma composed of 99% hydrogen, 1% carbon with an ion density of $5 \times 10^{14}\ cm^{-3}$. T_e was 20 eV for the spectrum on the left and 40 eV for the spectrum on the right.

4. PrismSPECT Simulations

Analysis of our experimental results was aided by the use of the non-LTE excitation kinematics code PrismSPECT (36), a scaled-down version of the Spect3D package utilized by Falk et al. (9). PrismSPECT features a relatively transparent graphical user interface and a wide variety of customizable options. Plasma properties such as temperature, density, and composition are specified by the user, and the code calculates a detailed model spectrum that can be compared to experimental results. A set of useful post processing tools are also available: the time evolution of the ionization balance for all plasma components can be monitered and displayed, as can the intensities of individual emission lines.

PrismSPECT does not assume LTE or coronal equilibrium (see chapter 2), instead it considers a full range of possible processes leading to atomic transitions. These include collisional excitation and de-excitation, spontaneous emission, photoexcitation and photoionization, stimulated emission, radiative recombination, collisional

ionization and recombination, autoionization, dielectronic recombination, and stimulated recombination. Multipliers can be set to alter the relative importance of each of these processes; for our simulations we let these equal one, since the default settings should best describe reality. PrismSPECT computes atomic level populations at each time step by solving equation 2.47, and the calculated transition rates are used to produce a model spectrum.

Examples of model spectra are shown in Figure 16. It is apparent that the spectra are dominated by carbon line emission. Notice also the sharp rise in the continuum around 900 Angstroms. This serves as clear evidence that radiative recombination is the dominant continuum process at work: recombinations to the hydrogen ground state produce photons with a minimum energy of 13.6 eV, corresponding to a wavelength of 911 Angstroms. At lower energies, there is decreased emission from recombination, since only recombinations to the $n = 2$ level and above will contribute.

4.1. Validity Checks

When using a highly customizable software package such as PrismSPECT, it is important to make sure the chosen simulation parameters produce self-consistent, physically reasonable results. Through a series of test simulations, we determined the optimal settings for accurately modeling the important physical processes in SSX while avoiding excessive computation time.

4.1.1. Atomic Models

PrismSPECT can in principle model radiative processes in a plasma of arbitrary composition. A companion program known as Atomic Model Builder (34) is used

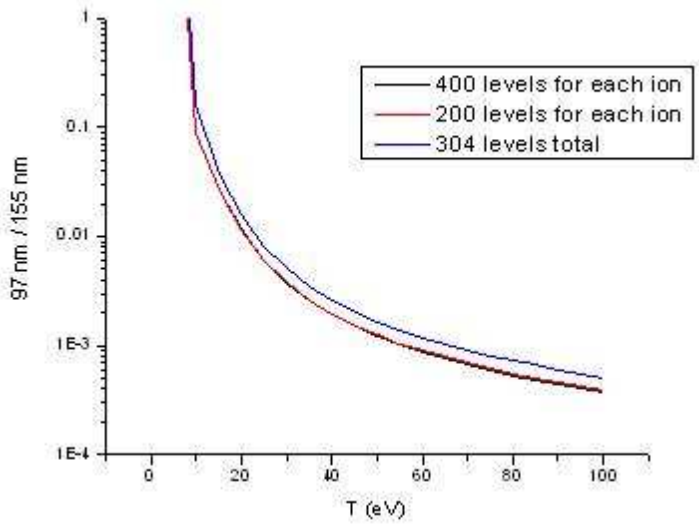

Fig. 17.— Temperature dependence of C III 97.7 nm / C IV 155 nm line ratio for three different carbon atomic models. Increasing the number of energy levels from 304 to 1061 (200 for each ion) significantly alters the line ratio at all temperatures, but a further increase to 1957 levels (400 for each ion) has only a negligible impact on simulation results.

to modify atomic models based on the ATBASE database (35). The full ATBASE atomic models are incredibly complex, so some degree of simplification is necessary in order to run simulations on a feasible timescale. For our applications, calculating exact populations for the atomic levels that feed important transitions was vital, so we used models with fine structure included. However, many of the higher energies levels of impurity ions produced no strong spectral features and could be ignored. When energy levels are left out of an atomic model, PrismSPECT does not simply ignore the electrons that would have populated those levels; rather, it allows them to populate the highest available levels, and then solves the standard rate equations to determine where they go from there.

Hydrogen in the SSX plasma is nearly 100% ionized, so for our simulations we

used an atomic model with only two energy levels–the ground state of the neutral atom, and the singly ionized state. Most of the line emission in the plasma comes from impurity ions, primarily carbon and oxygen. We ran a series of simulations to determine the number of energy levels we should include in these atomic models. Key spectral features (in particular, the C III 97.7 nm / C IV 155 nm line ratio) were seen to change as the number of energy levels in the carbon atomic model was increased from 304 to 1061 (200 levels for C I through C V, 60 for C VI, and one for C VII, the ionized state); however, further increases in the number of levels per ion produced only negligible changes in the model spectra (see Figure 17). We therefore concluded that 200 energy levels per carbon ion was sufficient for capturing the important atomic processes. A similar analysis revealed that 50 levels for O III through O VII and 1 level for the other ions was an ideal amount of detail for the oxygen atomic model. Fewer levels were needed for oxygen because it was only used for SXR calculations; since each filter passes many different emission lines, calculating the exact population of each energy level is less important for SXR than for calculations of temperature from individual line ratios.

4.1.2. Impurity Concentrations

Absolute impurity concentrations in SSX remain relatively unknown, although recent results (see Chapter 5) suggests that carbon is by far the dominant impurity, with oxygen present in smaller amounts. Fortunately, UV line intensity ratios for two lines produced by a single element should have little dependence on the element's concentration in the plasma. Furthermore, Swisher (2006) showed that SXR signal ratios are not effected by changes in the absolute concentrations of impurities, as long as their relative concentrations remain constant (41). Therefore, it suffices to

determine, for example, that carbon is ten times more abundant than oxygen in the SSX plasma. Such information can be estimated by comparing emission line strengths measured with the VUV monochromator to model spectra produced by PrismSPECT.

Simulations for interpreting the VUV monochromator data used a plasma composed of 99% hydrogen and 1% carbon. The primary temperature diagnostic used was the C III 97.7 nm / C IV 155 nm line ratio, so the inclusion of other impurities was unnecessary. For SXR simulations, on the other hand, leaving out impurities was not an option. Based on results outlined in Chapter 5, we assumed a carbon to oxygen abundance ratio of 1000/1 with negligible concentrations of other impurities such as nitrogen and metals. We therefore used a plasma with 98.999% hydrogen, 1% carbon, and 0.001% oxygen by number.

4.1.3. Justification for Using Steady-state Simulations

PrismSPECT can perform either steady-state, equilibrium simulations or time-dependent simulations in which the atomic rate equations are solved at every time step. The SSX plasma is undoubtedly not in a steady state during a shot. After the hydrogen gas is ionized, the plasma spends about 10 μs in the gun, with a density of approximately 8×10^{15} ions/cm^3. As it is ejected into the main vacuum chamber it expands and cools, eventually filling the entire volume with an average density of around 5×10^{14} ions/cm^3. Additional heating may occur later in the shot if magnetic reconnection takes place. Ideally, we would take advantage of PrismSPECT's ability to modify plasma parameters on-the-fly during time-dependent simulations. However, these simulations require extensive computational time, so from a practical standpoint it would be advantageous if we could rely on the simpler steady-state simulations to provide reasonably accurate results. Therefore, we ran a number of tests to assess

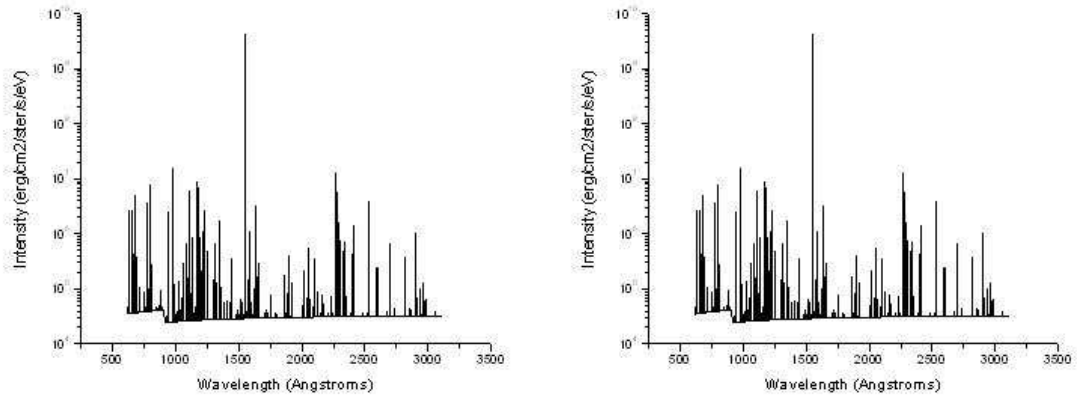

Fig. 18.— Left: Model spectrum from a steady-state simulation with T = 30 eV and n = 5×10^{14} ions/cm^3. Right: Model spectrum at t = 50 μs during a time-dependent simulation with T = 30 eV, starting atomic levels populations calculated based on LTE at 0.025 eV (room temperature) and n = 8×10^{15} ions/cm^3 during the first 10 μs of the run, decreasing linearly to 5×10^{14} ions/cm^3 over the next 20 μs (so at 50 μs both plasmas have the same temperature and density). The two spectra are essentially indistinguishable.

the differences between steady-state and time-dependent simulations.

Although a steady-state simulation cannot possibly capture the behavior of the SSX plasma as it ionizes in the gun and is ejected into the flux conserver, our simulations need only replicate the plasma conditions seen by the VUV monochromator and SXR. This is a somewhat easier task, since both diagnostics observe the plasma through the center of the vacuum chamber (see Figure 5). By the time the plasma reaches the center and can be seen, its initial transitive properties may have stabilized. VUV monochromator and SXR signals typically are zero for roughly the first 30 μs of a shot and peak around t = 50-60 μs. Therefore, the relevant comparison for our purposes is between steady-state and time-dependent simulations at t = 50 μs. As shown in Figure 18, the model spectra for time-dependent and steady-state simulations are qualitatively nearly identical.

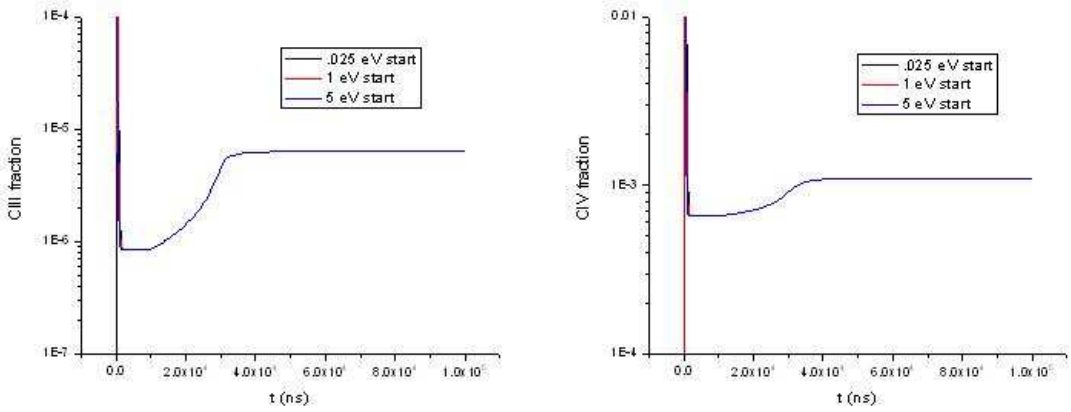

Fig. 19.— Evolution of C III (left) and C IV (right) fractions in simulations with T = 30 eV, nominal SSX density (8×10^{15} ions/cm^3 in the gun, decreasing linearly to 5×10^{14} ions/cm^3 at t = 30 μs) and starting atomic level populations calculated based on LTE at three different starting temperatures. The three simulations become nearly identical within less than 10 μs.

To determine the time needed for a plasma like that in SSX to reach a relatively steady state, we ran time-dependent simulations with typical SSX densities (8×10^{15} ions/cm^3 in the gun, decreasing linearly to 5×10^{14} ions/cm^3 at t = 30 μs) and temperatures (30 eV) and variable initial conditions. Figure 19 shows that the initial atomic level populations have no measurable effect on the plasma conditions at times later than 10 μs. The insensitivity to initial conditions is also evident in Table 1, which presents the carbon emission line strength ratios at t = 50 μs for the same set of simulations. The short time needed to reach equilibrium demonstrates that steady-state simulations are sufficient to achieve accurate results at SSX densities.

A quick analytical calculation of the mean excitation time in the SSX plasma confirms that the equilibration time will be small compared to the length of a shot. Consider an electron moving through the plasma with velocity v_e. If n is the ion density and σ is the electron's interaction cross section with the ions, then the electron

Table 1: Simulated carbon emission line ratios at t = 50 μs

Simulation Type	C III 97.7 nm / C IV 155 nm	C III 229.7 nm / C IV 155 nm
Steady State	3.765×10^{-3}	1.686×10^{-4}
0.025 eV start	3.766×10^{-3}	1.686×10^{-4}
1 eV start	3.766×10^{-3}	1.686×10^{-4}
5 eV start	3.766×10^{-3}	1.686×10^{-4}

will effectively pass through volume at a rate equal to $v_e\sigma$, so the time after which we can expect the electron to interact with one ion is given by:

$$v_e\sigma t = \frac{1}{n} \tag{4.1}$$

The electron's velocity can be calculated if we know the electron temperature:

$$\begin{aligned} \frac{1}{2}m_e v_e^2 &= \frac{3}{2}kT \\ v_e &= \sqrt{\frac{3kT}{m_e}} \end{aligned}$$

So the problem becomes one of knowing the correct interaction cross section to use. Osterbrock (31) gives the excitation cross section for electron velocities above the threshold for excitation to be:

$$\sigma_{12}(v_e) = \frac{\pi\hbar^2\Omega(1,2)}{m_e^2 v_e^2 \omega_1} \tag{4.2}$$

where $\Omega(1,2)$ is the collision strength, which varies for different ions but is of order unity, and ω_1 is the statistical weight of the lower energy level for a particular

transition (also of order unity). Ignoring these factors, we are left with:

$$\sigma_{12}(v_e) \approx \frac{\pi\hbar^2}{m_e^2 v_e^2} \tag{4.3}$$

$$\sigma v_e \approx \frac{\pi\hbar^2}{m_e^2 v_e} = \frac{\pi\hbar^2}{m_e^2}\sqrt{\frac{m_e}{3kT}} \tag{4.4}$$

$$t\pi\hbar^2\sqrt{\frac{1}{3kTm_e^3}} = \frac{1}{n} \tag{4.5}$$

$$t = \frac{\sqrt{3kTm_e^3}}{n\pi\hbar^2} \tag{4.6}$$

For a density $n = 5 \times 10^{14}$ ions/cm^3 and electron temperature $T_e = 30$ eV, the mean excitation time is then:

$$t = \frac{\sqrt{(3)(30\,eV)(.511 \times 10^6\,eV)^3}}{(5 \times 10^{14}\ cm^{-3})\pi(197.327 \times 10^{-7}\,eV\,cm)^2(c)} \tag{4.7}$$

$$t = 2 \times 10^{-7}\,s \tag{4.8}$$

Therefore, in a period of several μs, each ion in SSX will be collisionally excited many times, with the result being that equilibrium will be reached on a time scale short enough to allow us to ignore the time-dependence of quantities in our PrismSPECT simulations. Of course, our ultimate goal is to derive a time-dependent electron temperature profile for each shot, but this can be achieved by running steady-state simulations and then comparing the model spectra to data at each time step.

4.2. Calculation of T_e from VUV line ratios

Using PrismSPECT to interpret the VUV monochromator data was reasonably straightforward. Rather than attempting to vary plasma temperature and density during a single simulation in such a way as to match the observed time evolution of line strength ratios, we ran steady-state simulations for a number of different electron temperatures and then chose the temperature that best fit the data at each time step.

Simulated line ratios showed some density dependence, so we repeated the calculations for three different ion densities: 1×10^{14} cm^{-3}, 5×10^{14} cm^{-3}, and 2×10^{15} cm^{-3}. HeNe interferometer data implies a typical density of $4 - 5 \times 10^{14}$ cm^{-3} during the 30-100 μs time interval of an SSX shot.

VUV monochromator data was processed and compared to simulation results using a code written by the author in IDL. The monochromator trace for each shot was smoothed over 1 μs intervals, and signals for a number of shots looking at the same spectral line were averaged. This average signal was then divided by the average signal for a different spectral line to determine an average line ratio at each time step. The average plasma temperature at each time step was calculated by finding the best possible match between simulated and measured line ratios. The need to average over many shots is the primary disadvantage of this method for determining the electron temperature.

4.3. Calculations of T_e from SXR data

Interpreting SXR data is significantly more complicated, but the potential rewards are great: once a complete set of PrismSPECT simulations have been run and a fitting code has been written, it should be possible to calculate a temperature profile within minutes after a given shot, thereby allowing experimental parameters to be adjusted on the fly to achieve the desired plasma properties (for example, a very hot plasma). Simulations were run for a range of electron temperatures between 5 eV and 100 eV. For each model spectrum, we used the known SXR filter responsivities (see Figure 12) to calculate the signal that would have been registered by each of the four diodes had the simulated plasma been produced in SSX. These simulated filter signals were then compared to the experimentally measured filter signals, smoothed

over 1 μs intervals. We derived a temperature profile by minimizing the chi-squared statistic at each time step to determine the model spectrum that best fit the data.

Calculating the SXR signals that a given model plasma would produce is non-trivial and warrants furthur discussion. Planar PrismSPECT simulations produce model spectra with units of specific intensity (I), or erg/cm^2/ster/s/eV. In order to calculate the signal that a given model spectrum would produce in each of the SSX soft x-ray detector (SXR) filters, we must convert from intensity to W/eV, since the filter responsivities are given in A/W and the SXR output is a current measured in A. The first step is a straightforward conversion from erg/s to W:

$$I\ (erg/cm^2/ster/s/eV) \times (1 \times 10^{-7}\, W{\cdot}s/erg) = I\ (W/cm^2/ster/eV) \tag{4.9}$$

Next we need to multiply by a solid angle. By a theorem of geometric optics, etendue is conserved throughout an optical system, so the solid angle we must choose is the angle Ω seen by the detector. In SSX this angle is limited by the smallest hole through which light must pass on its way from the flux conserver to the SXR.

If r is the radius of the hole and d is the distance from the light-collecting diode to the hole, then in the small angle approximation, the solid angle seen by the detector is given by:

$$\Omega = \int_0^{2\pi} \int_0^{\theta} cos\theta sin\theta d\theta d\phi \approx \int_0^{2\pi} \int_0^{\theta} \theta d\theta d\phi \tag{4.10}$$

$$\Omega = 2\pi \times \frac{\theta^2}{2} = \pi(\frac{r}{d})^2 \tag{4.11}$$

$$I\ (W/cm^2/ster/eV) \times (\Omega\ ster) = I\ (W/cm^2/eV) \tag{4.12}$$

Now I has units of flux. To convert to power, we multiply by the area S of the detector's light-collecting surface:

$$I\ (W/cm^2/eV) \times (S\, cm^2) = I\ (W/eV) \tag{4.13}$$

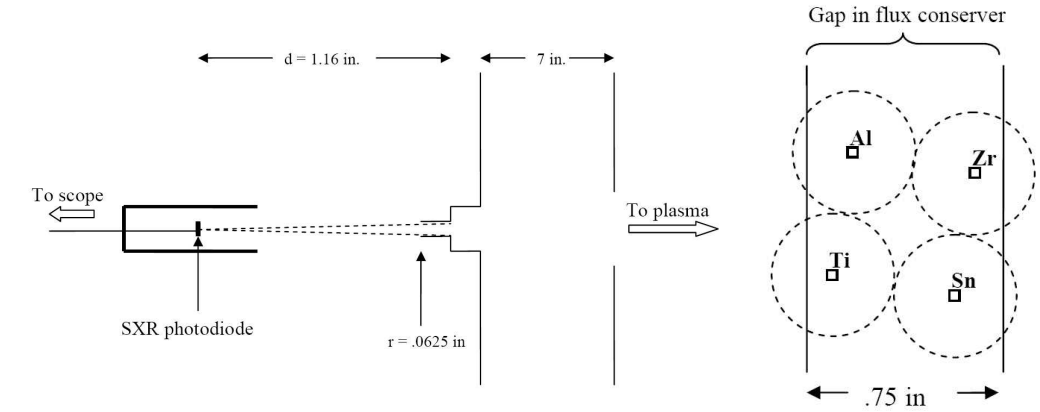

Fig. 20.— SXR Lines of Sight. As shown in the left figure, the solid angle that each photodiode sees is limited by the small gap of radius 0.0625 inches that photons must pass through on their way from the plasma to the detector. Beyond this segment, the line of sight of each photodiode is truncated slightly by the edge in the gap in the flux conserver. The figure on the right shows that the magnitude of the solid angle seen differs slightly for each photodiode (dotted circles represent the solid angle seen by each photodiode in the direction of the flux conserver).

For SSX, $r = .0625$ in and $d = 1.16$ in (see Figure 20), so $\Omega = 9.12 \times 10^{-3}$ ster. $S = .01$ cm^2, so the total conversion factor is:

$$(.00912)(.01) = 9.12 \times 10^{-5} \tag{4.14}$$

Now we can multiply the spectral intensities by the filter responsivities at each energy to determine that fraction of the spectrum that each SXR channel registers. The PrismSPECT output is binned at varying energy intervals, with more points at energies where emission lines appear. Reporting the spectral intensity in terms of power/eV assures that each bin will be given the proper weight. In order to calculate the total signal through each SXR filter, we must integrate over the entire range of energies in the spectrum:

$$(Current\,in\,A) = \int_0^\infty (Power\,in\,W/eV)(Responsivity\,in\,A/W)d(eV) \tag{4.15}$$

Numerically, this integration is accomplished by assuming the spectrum has a constant value in each of the energy bins and summing the product of the power in W/eV, the filter responsivity, and the bin size at each data point.

One other complication must be mentioned. As shown in Figure 20, the gap in the flux conserver is only .75 inches wide, so the sight line of several of the SXR filters may be somewhat obscured. This will effect the filter signals by less than a factor of two, so keeping in mind the large uncertainties in other input parameters used for our SXR temperature derivations, we have ignored it for the time being. However, a more detailed ray-tracing analysis should be carried out to ensure the accuracy of SXR results.

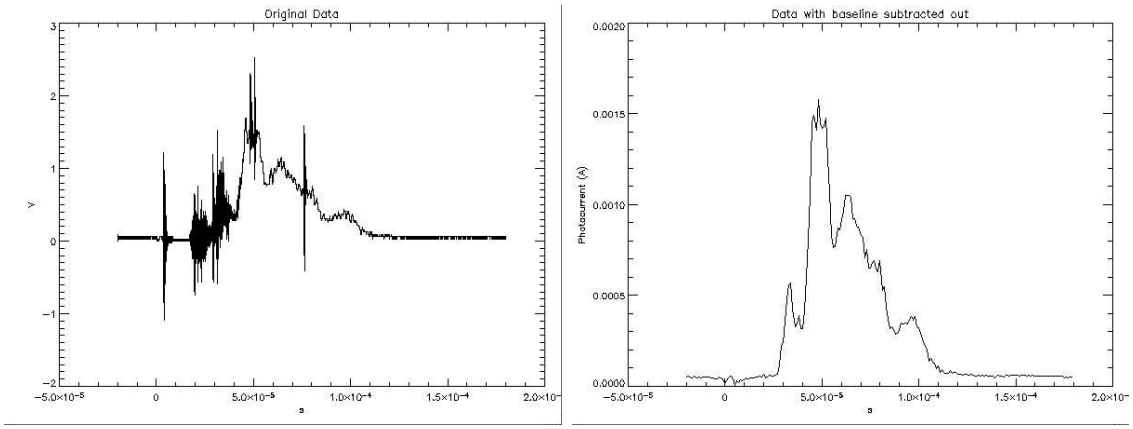

Fig. 21.— Sample VUV monochromator data for an observation of the C IV 155 nm line during an SSX shot with counter-helicity spheromak merging. Left: Raw data. Right: Data with baseline signal subtracted out, smoothed over 1 μs intervals.

5. Results and Discussion

5.1. Results from the VUV monochromator

5.1.1. Lines Observed and Impurity Concentrations

Comparisons of PrismSPECT simulations with data taken with the monochromator produced several notable results. Using simulations with equal concentrations of carbon, nitrogen, and oxygen impurities as our guide, we looked for the C, N, and O emission lines expected to be strongest in an SSX spectrum. The results are summarized in Table 2. Five emission lines produced signals that could be reliably distinguished from background noise: C III 97.7 nm, C IV 155 nm, C III 229.7 nm, N IV 124 nm, and O V 63.0 nm. The strongest line observed was C IV 155 nm; it consistently produced PMT currents of over 1 mA. At first glance this fact might seem unusual–C V is the dominant carbon ionization stage in SSX (see Figure 22), so we might naively expect a C V line to be strong. However, the resonance lines for C V (lines produced by a transition to the ground state) are in the 3-4 nm range (see

Appendix A), well below the wavelength range the VUV monochromator can detect. Transitions between excited states are far less frequent, so our non-detection of the C V 227.4 nm line is not surprising. The C IV 155 nm line, on the other hand, is a resonance line, as is the C III 97.7 nm line.

Table 2: Impurity Emission Lines Observed with the VUV monochromator

Ion	Wavelength	Transition	Typical Signal
C III	97.7 nm	$1s^2 2s^1 2p^1\ ^1P_1 \rightarrow 1s^2 2s^2\ ^1S_0$	10 μA
C IV	155 nm	$1s^2 2p^1\ ^2P_{1/2}$ & $^2P_{3/2} \rightarrow 1s^2 2s^1\ ^2S_{1/2}$	1-2 mA
C V	227.4 nm	$1s^1 2p^1\ ^3P_0$ & $^3P_1$ & $^3P_2 \rightarrow 1s^1 2s^1\ ^3S_1$	not detected
C III	229.7 nm	$1s^2 2p^2\ ^1D_2 \rightarrow 1s^2 2s^1 2p^1\ ^1P_1$	10 μA
N IV	76.5 nm	$1s^2 2s^1 2p^1\ ^1P_1 \rightarrow 1s^2 2s^2\ ^1S_0$	not detected
N V	124 nm	$1s^2 2p^1\ ^2P_{1/2}$ & $^2P_{3/2} \rightarrow 1s^2 2s^1\ ^2S_{1/2}$	100 μA
O IV	55.4 nm	$1s^2 2s^1 2p^2\ ^2P_{1/2}$ & $^2P_{3/2} \rightarrow 1s^2 2s^2 2p^1\ ^2P_{1/2}$ & $^2P_{3/2}$	not detected
O V	63.0 nm	$1s^2 2s^1 2p^1\ ^1P_1 \rightarrow 1s^2 2s^2\ ^1S_0$	5-10 μA
O VI	79 nm	$1s^2 2s^1 2p^2\ ^2D_{3/2}$ & $^2D_{5/2} \rightarrow 1s^2 2s^2 2p^1\ ^2P_{3/2}$	not detected
O VI	103.5 nm	$1s^2 2p^1\ ^2P_{1/2}$ & $^2P_{3/2} \rightarrow 1s^2 2s^1\ ^2S_{1/2}$	not detected

The oxygen lines featured in Table 2 are also resonance lines. Analogies can be drawn between the O V 63.0 nm line and the C III 97.7 nm line, and also between the O VI 103.5 nm line and the C IV 155 nm line, as each pair corresponds to identical electron transitions within ions that share a common structure. Oxygen's ionization balance at SSX temperatures is more evenly distributed than carbon's; although O VII is the dominant ion at T $>$ 30 eV, O IV, O V, and O VI are all present in appreciable fractions.

The comparative strengths of oxygen and carbon lines can yield information about the relative fractions of these impurities present in SSX. Carbon to oxygen line ratios depend on temperature, the very variable this research is trying to constrain, so

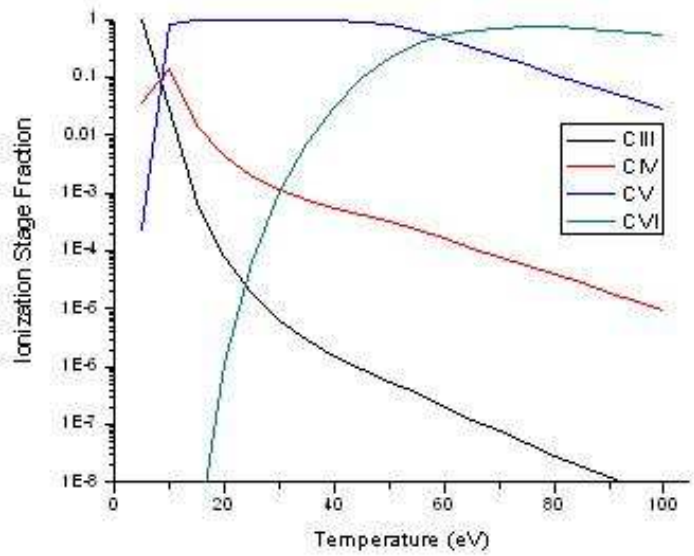

Fig. 22.— Carbon ionization balance in equilibrium for PrismSPECT simulations with $n = 5 \times 10^{14}$ $ions/cm^3$ (a typical SSX density). C V is the dominant ion for temperatures between 10 and 60 eV; the C III and C IV abundances are several orders of magnitude lower.

a precise determination of impurity concentrations will likely never be realized using this method. Nevertheless, comparisons of experimental data to PrismSPECT simulations can certainly help us improve our estimates of these concentrations, thereby increasing the accuracy and relevance of future simulations (determination of relative impurity concentrations is of great important to SXR modeling, since SXR filter ratios depend on large-scale spectral features rather than individual line intensities).

The strongest oxygen line in our PrismSPECT simulations is O V 63.0 nm. As shown in Figure 23, we would expect this line's intensity to be several orders of magnitude greater than that of the C III 97.7 nm line if carbon and oxygen were present in equal concentrations in SSX. Instead, we see signals on the order of 10 μA for both lines. The other oxygen lines listed in Table 2 also appear stronger than the

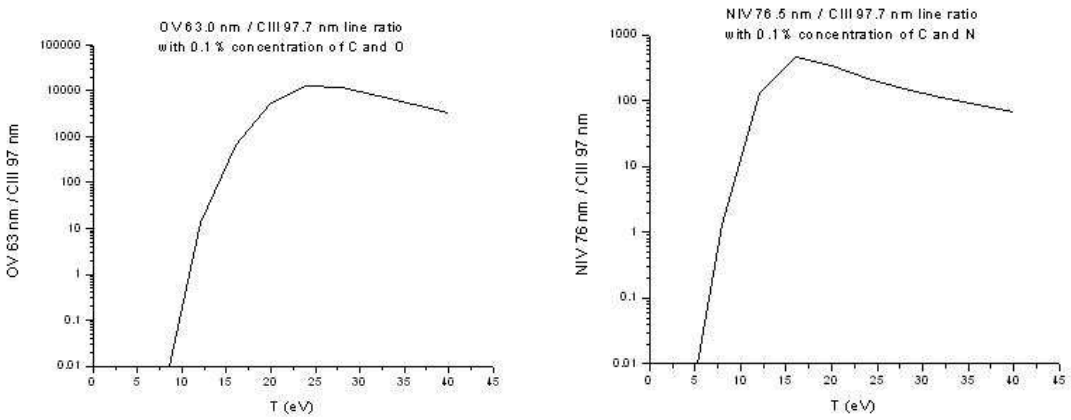

Fig. 23.— Line ratios calculated from PrismSPECT simulations with 0.1% carbon, nitrogen, and oxygen impurities. The N IV 76.5 nm line is predicted to be over 100 times stronger than the C III 97.7 nm line for plausible SSX temperatures, and the O V 63.0 nm line is predicted to be over 1000 times stronger. However, in the VUV monochromator data, the 97.7 nm and 63.0 nm line strengths are approximately equal, and the 76.5 nm line is not detected. These results allow us to place an upper limit on the concentrations of nitrogen and oxygen relative to carbon in the SSX plasma.

C III 97.7 nm line in PrismSPECT simulations, but we failed to detect them at all with the monochromator. These results imply that there is significantly more carbon than oxygen in the SSX plasma. We have adapted a C/O number density ratio of 1000/1 for SXR simulations.

A similar analysis can be applied to the nitrogen impurity concentration. Figure 23 shows that the N IV 76.5 nm / C III 97.7 nm line ratio is approximately 100/1 for temperatures between 15 and 45 eV. The N IV 76.5 nm line could not be detected using the VUV monochromator, so the nitrogen concentration in the SSX plasma is probably extremely low. We must question this result somewhat because of the strong signal observed from the N V 123.9 nm line (see Table 2). However, data for this line may be suspect because of its proximity to the hydrogen recombination line Lyman

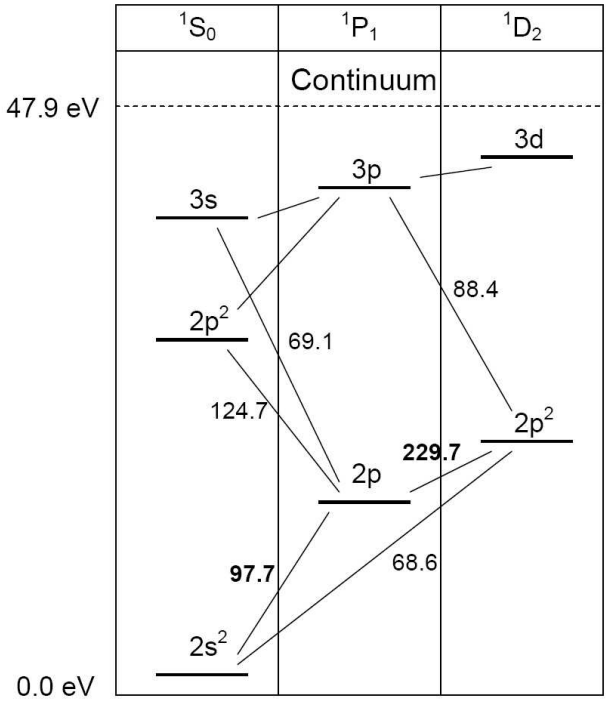

Fig. 24.— Partial carbon III energy level diagram.

α at 121.6 nm. Attempts to isolate the 123.9 nm line and Lyman α separately were promising but not entirely conclusive, so we must consider the possibility that the 123.9 nm measurement was contaminated. This conclusion seems rather likely given the disagreement between the 76.5 nm and 123.9 nm line measurements. Further observations of nitrogen lines will be required to settle the issue, but for now we are assuming a nitrogen-free plasma for SXR calculations.

5.1.2. Anomalous 229.7 nm Line Strength

The C III 229.7 nm line is produced by a transition between excited states in the C III atom–as shown in Figure 24, the lower level of the transition is the upper level of the 97.7 nm transition. Therefore, we might expect the 229.7 nm line to be

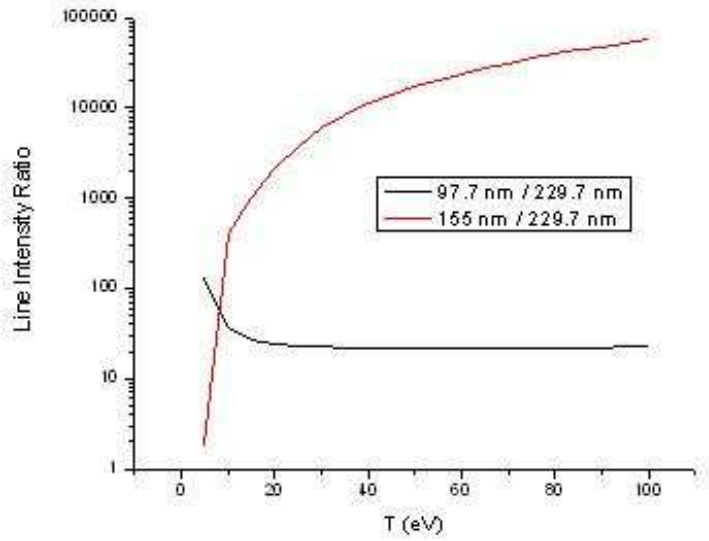

Fig. 25.— Simulated line ratios involving C III 229.7. The 97.7 nm / 229.7 nm ratio is approximately constant at 22 for temperatures between 20 and 100 eV. There are no temperatures between 5 and 100 eV for which the simulation replicates the experimental finding of an approximately 1:1 ratio between the 97.7 nm and 229.7 nm lines.

relatively weak in the SSX plasma. PrismSPECT simulations support this hypothesis; as shown in Figure 25, the 97.7 nm / 229.7 nm line ratio is at least 20/1 for all plasma temperatures between 5 and 100 eV. However, VUV monochromator data (see Table 2) suggest that the 229.7 nm and 97.7 nm lines have similar intensities in SSX. This anomaly stands as one of the unsolved mysteries unearthed by our research.

Several factors rule out errors in measurement or data interpretation as a possible cause of the discrepency between simulation and experiment. The C III 229.7 nm line has been known to be strong in SSX for some time–measurements of ion temperature and bulk flows using ion Doppler spectroscopy (IDS) have focused exclusively on this line, relying on the intensity of the spectral feature to make detailed measurements of bi-directional jets produced by magnetic reconnection (5). Furthermore, as noted

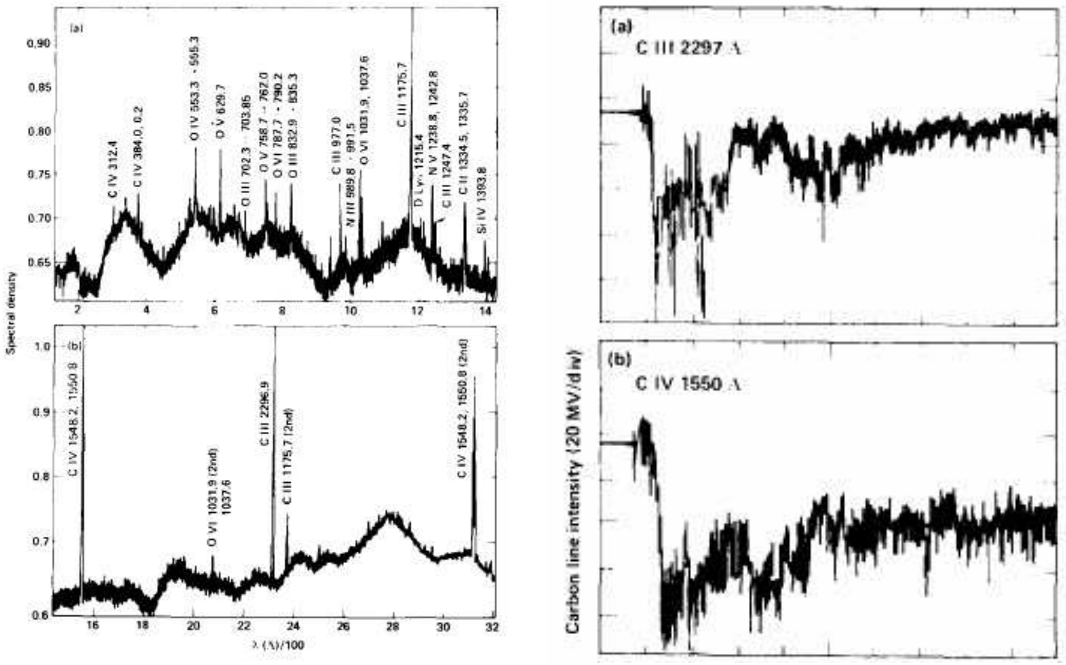

Fig. 26.— Spectral data from Turner et al. (1983). Left: Readings from the VUV spectrum taken with a 1 m grazing incidence spectrograph. Right: C III 229.7 nm and C IV 155 nm line emission versus time, measured with a VUV monochromator (43).

in Chapter 3, Lukin (2000) (26) found that the 229.7 nm / 97.7 nm ratio was approximately 10 times larger than expected. Most importantly, a strong 229.7 nm line has been independently observed in at least two other spheromaks.

Turner et al. (1983) (43) describe the results of spheromak experiments at the Beta II facility at the Lawrence Livermore National Laboratory (LLNL). For an electron temperature of approximately 10 eV, the strongest impurity emission lines observed were C III 117.5 nm, C IV 155 nm, and C III 229.7 nm. Of particular relevance to the present discussion is the fact that the 229.7 nm line was stronger than the C III 97.7 nm line. Several oxygen and nitrogen lines were also observed, but lines from metal ions such as Ni II, Fe II, and Cu II that might have been released from the

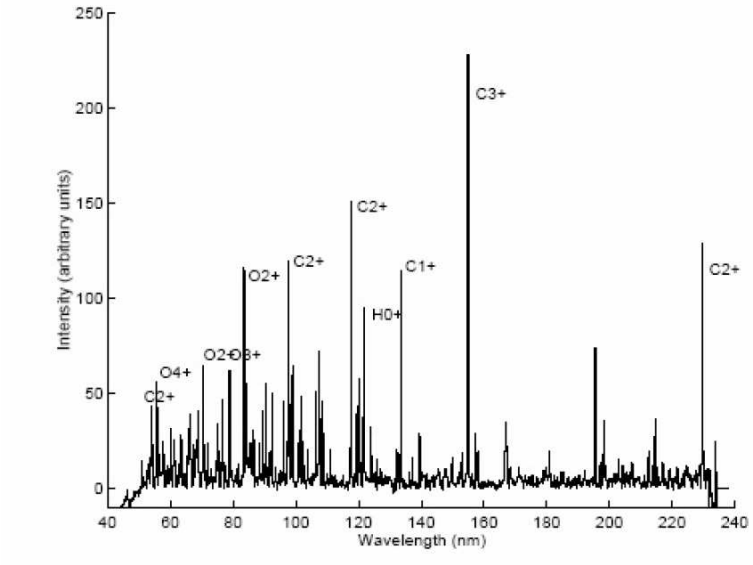

Fig. 27.— Densitometer trace of film spectrographs in the VUV from Cunningham (1997) (8). As in the case of the Turner spectrum, intensity calibration may be an issue when comparing line strengths.

gun or flux conserver walls were absent. VUV monochromator data (see Figure 26) suggests that the C IV 155 nm line was less than 10 times stronger than the C III 229.7 nm line, although the authors stop short of estimating a line ratio because the monochromator was not absolutely calibrated (neither is our instrument at SSX–see Chapter 3).

Results from the SPHEX spheromak presented by Cunningham (1997) (8) also demonstrate a strong C III 229.7 nm line. Calculated electron temperatures are hotter–around 50-100 eV–but the results are the same: as shown in Figure 27, the 97.7 nm and 229.7 nm lines appear to have similar intensities. Cunningham cautions that his spectrum should be regarded as purely qualitative, since the VUV film processing regime was not well controlled.

Neither paper addresses the issue of an anomalously strong C III 229.7 nm line, although in light of Figure 24, a line intensity equal to or greater than that of the

97.7 nm line at any temperature is clearly unusual. Such a phenomenon could only occur if electrons were collisionally excited out of the 2p level before they had time to make the transition back to the ground state. The fact that C III is a subdominant ionization stage in the plasmas considered may be important. If collisional excitation from the ground state were the primary mechanism populating the upper levels of C III, then we would expect the 97.7 nm line to be more intense than the 229.7 nm line. If, on the other hand, recombination were the dominant populating mechanism, then we might expect a typical electron to cascade down to the ground state and emit photons at both 229.7 nm and 97.7 nm, allowing the two lines to have comparable strengths. Of course, this argument neglects the fact that there are three downward electron transitions that can populate the 2p level in C III, and only one of these leads to emission at 229.7 nm. Furthermore, at $T_e \approx 10$ eV, as in the LLNL experiments, C III in fact makes up at least 10% of the total carbon (see Figure 22).

5.1.3. Electron Temperature Determination

Given the anomalous strength of the C III 229.7 nm line and the lack of detectable oxygen or nitrogen lines, the C III 97.7 nm / C IV 155 nm line ratio provided us with our most reliable diagnostic of electron temperature. The temperature dependence of this line ratio as calculated by PrismSPECT simulations using three different ion densities is shown in Figure 28. For a plasma in coronal equilibrium, emission line ratios should not depend on density. However, PrismSPECT simulations show that the 97.7 nm / 155 nm line ratio does depend on density at the temperatures and densities present in SSX. This density dependence could be a sign that the coronal approximation begins to break down at densities as low as 10^{14} ions/cm^3, or it may be a function of the fact that C III and C IV are subdominant ion stages at T $>$ 10

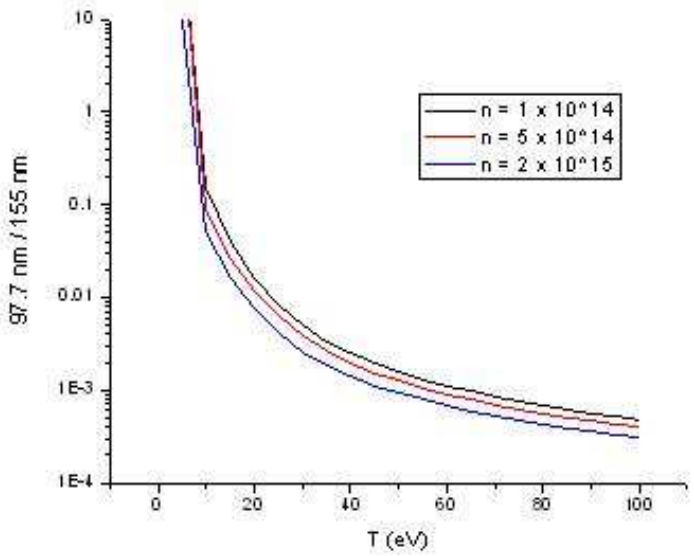

Fig. 28.— Simulated C III 97.7 nm / C IV 155 nm line strength ratio plotted as a function of temperature for three different plasma densities.

eV (see Figure 22), so small absolute changes in their abundances can correspond to large relative changes that significantly alter the line ratio of interest.

Figure 29 shows the electron temperatures we derived for counter-helicity merging shots by comparing the average measured 97.7 nm / 155 nm line ratio to the simulated line ratios calculated by PrismSPECT. Assuming a low ion density leads to a high temperature estimate and vice versa, as we would expect from Figure 28. HeNe interferometer measurements suggest that the typical density in SSX is around $4-5\times10^{14}$ ions/cm^3, so the upper plot in the figure probably gives the most accurate average temperature profile. Large shot-to-shot variation means that our uncertainty range (calculated by finding the standard deviation of the signal at each time step for each line and then propogating error) is fairly large–we can determine T_e to within only about 5 or 10 eV. Increasing the sample size by taking more data will be useful for bringing this uncertainty down.

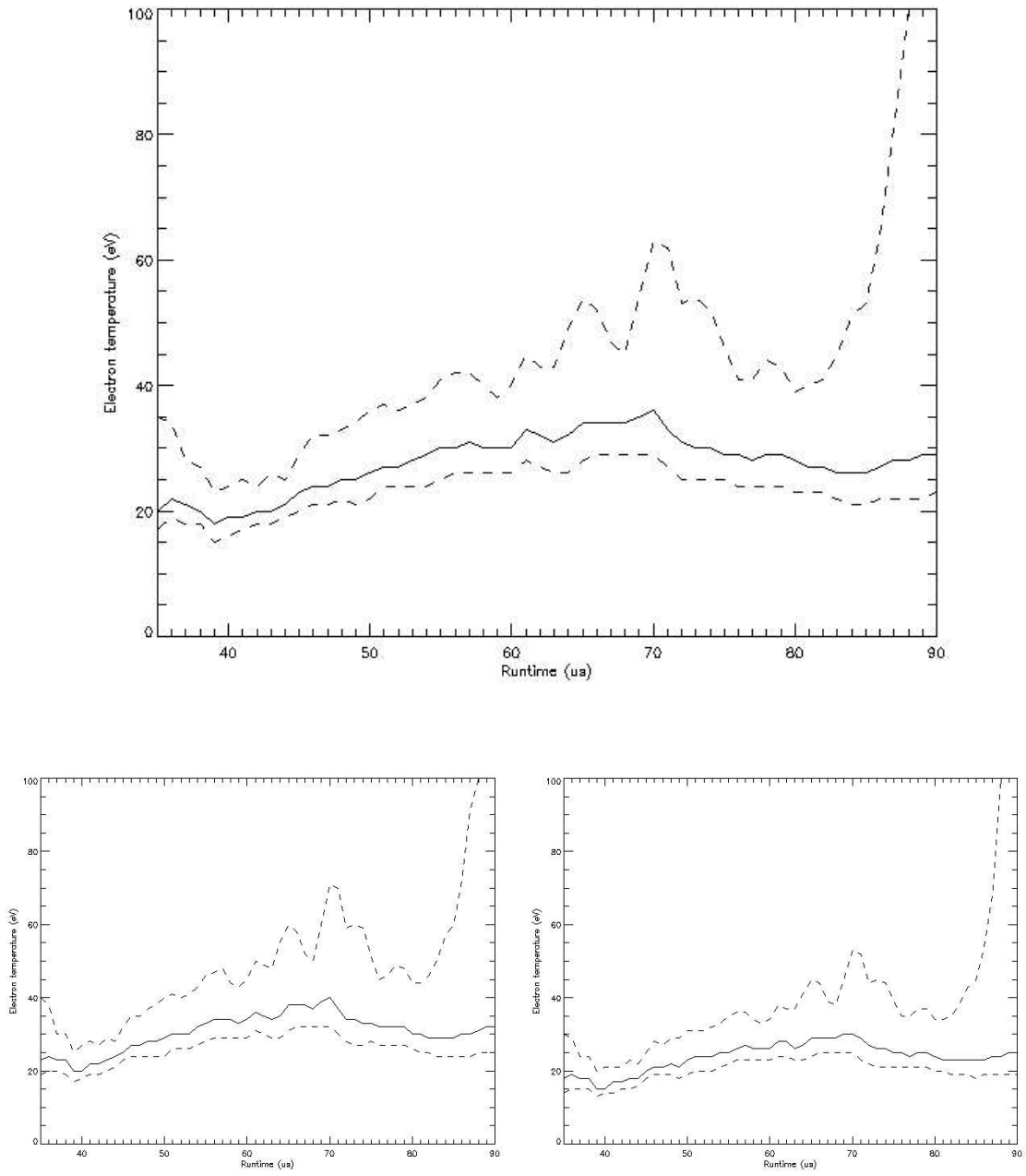

Fig. 29.— SSX electron temperature during counter helicity merging. Dotted lines give the uncertainty range. Temperature profiles were derived from the 97.7 nm / 155 nm line ratio averaged over 25 shots for each line, assuming a plasma density of 5×10^{14} ions/cm^3 (top), 1×10^{14} ions/cm^3 (lower left), and 2×10^{15} ions/cm^3 (lower right). The actual ion density in SSX has been previously measured to be $4-5 \times 10^{14}$ ions/cm^3.

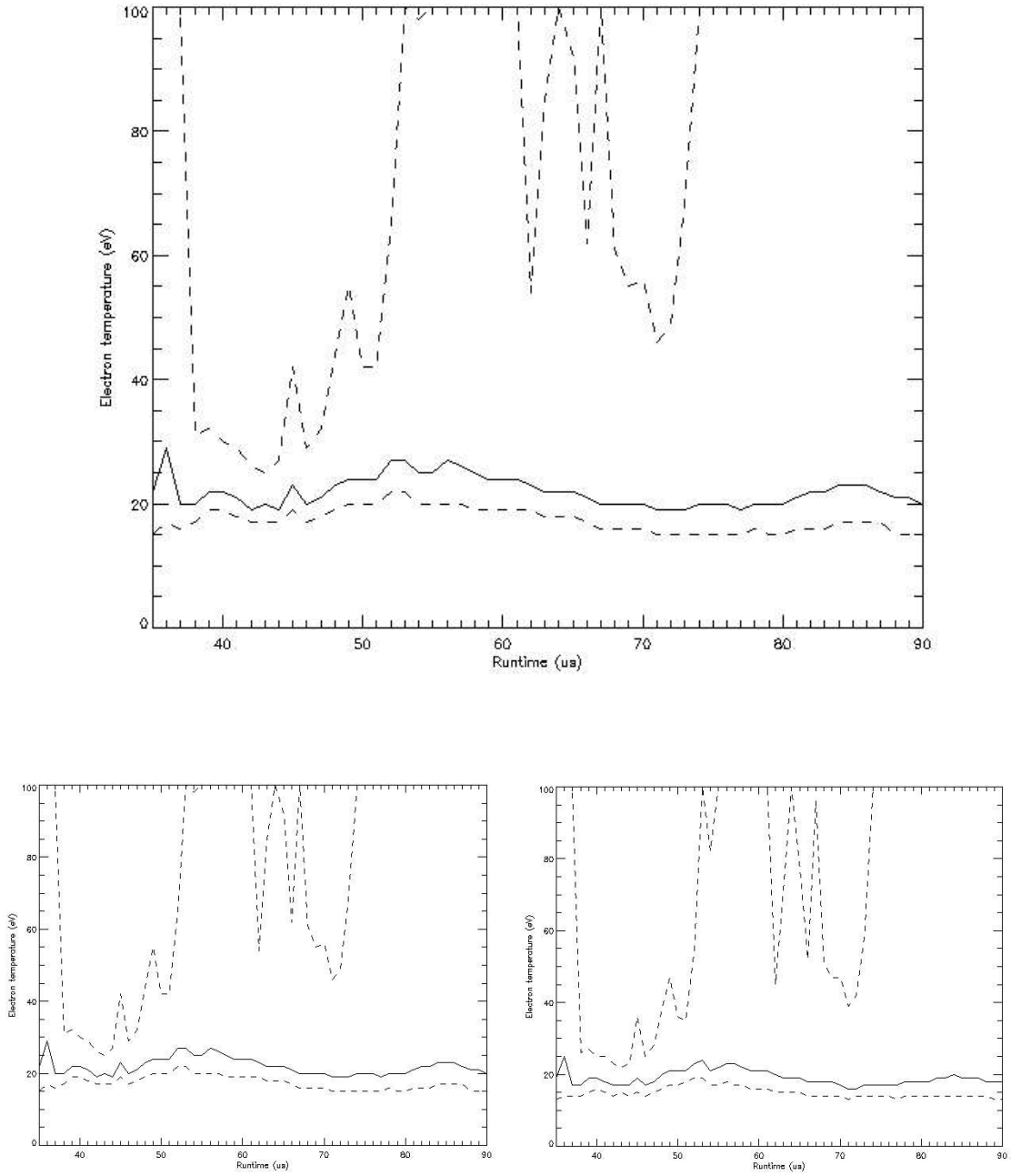

Fig. 30.— SSX electron temperature during single spheromak shots. Dotted lines give the uncertainty range. Temperature profiles were derived from the 97.7 nm / 155 nm line ratio averaged over 25 shots for each line, assuming a plasma density of 5×10^{14} ions/cm^3 (top), 1×10^{14} ions/cm^3 (lower left) and 2×10^{15} ions/cm^3 (lower right).

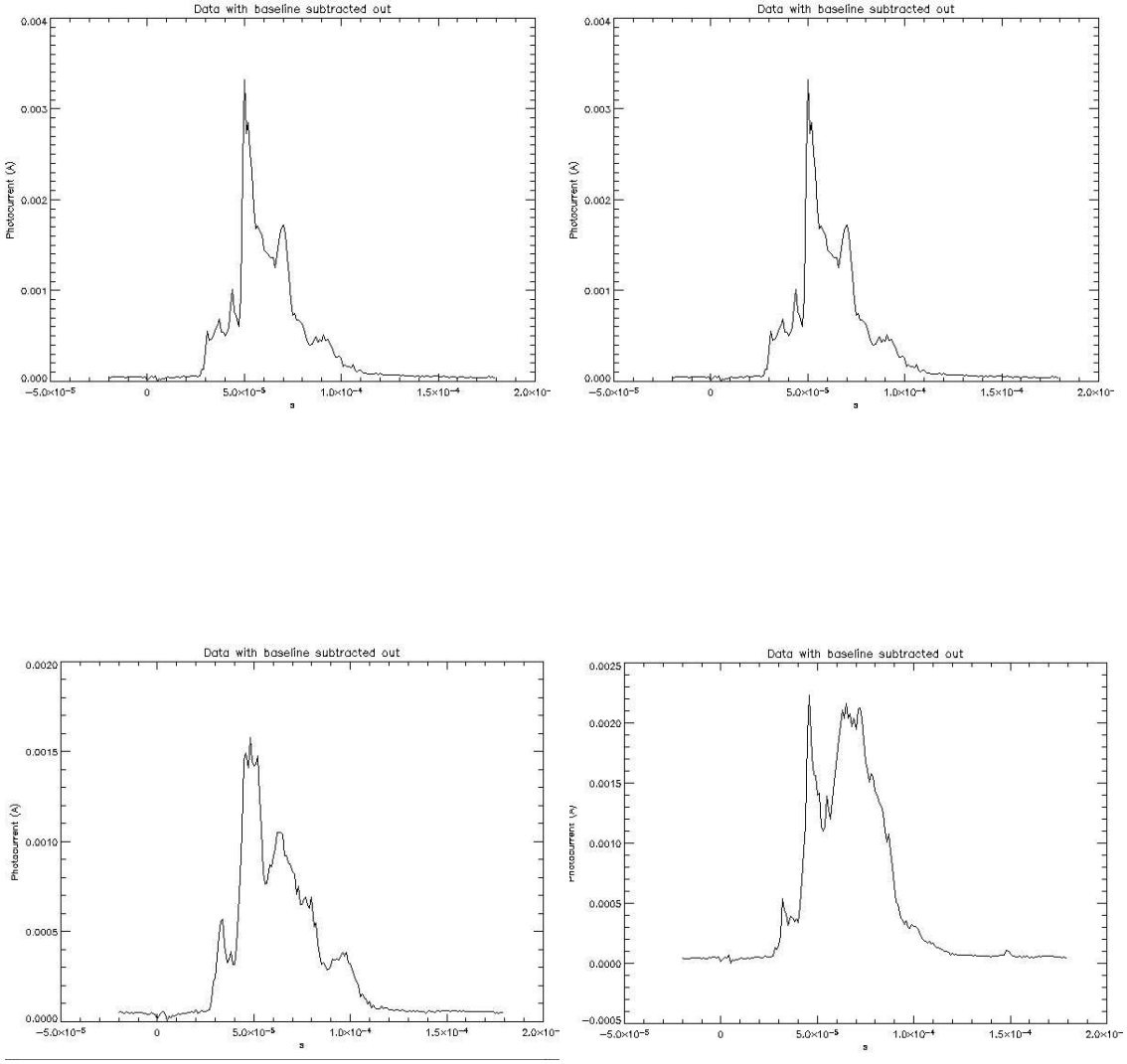

Fig. 31.— VUV monochromator measurements of the C IV 155 nm line from four consecutive counter-helicity merging shots on August 2, 2006. There is a consistent peak at around t = 50 μs, but the other qualitative features of the signal differ substantially from shot to shot. These differences probably correspond to variations in the timing and intensity of magnetic reconnection. Therefore, it is possible that by averaging the data over many shots, we may have smoothed out the temperature profile and lost evidence of a strong temperature peak associated with reconnection.

For shots in which two counter-helicity spheromaks merge, we would expect heat to be released and temperatures to rise during magnetic reconnection. Indeed, we see in Figure 29 that the average electron temperature gradually climbs from approximately 20 eV early in the shot to 30-35 eV at t = 60-70 μs. However, it is at this point in the analysis that the need to average over many shots when calculating temperatures using the VUV monochromatorbecomes problematic. As shown in Figure 31, the timing of reconnection varies somewhat from shot to shot due to the complex plasma dynamics in SSX. Therefore, if there were a more drastic temperature peak associated with reconection, it may have been smoothed over in our final temperature profiles. SXR measurements should help to resolve the issue; once the system is optimized, we will be able to calculate electron temperatures for individual shots.

We also calculated the average temperature for single spheromak shots; this is shown in Figure 30. If the rise in temperature during counter helicity shots were indeed due to the release of magnetic energy, we would expect such a feature to be absent in the single spheromak temperature profile, since no magnetic reconnection takes place during these shots. Unfortunately, the uncertainty on the single-spheromak temperature profile is enormous, so it is difficult to draw any strong conclusions from the data. It does appear that the temperature is relatively constant at $T \approx 20$ eV between t = 35 μs and t = 55 μs.

The large uncertainty in the single spheromak measurement may be a result of large shot-to-shot variations caused by perturbations from a Mach probe experiment running on the same day, in which case taking more data should solve the problem. However, Falk (9) points out that an FRC, the configuration formed when two spheromaks merge, is a more stable configuration than a spheromak, so it is possible that the single spheromak is already beginning to decay at t = 55 μs. Notice in Figure 29 that the temperature uncertainty for counter-helicity shots skyrockets around t

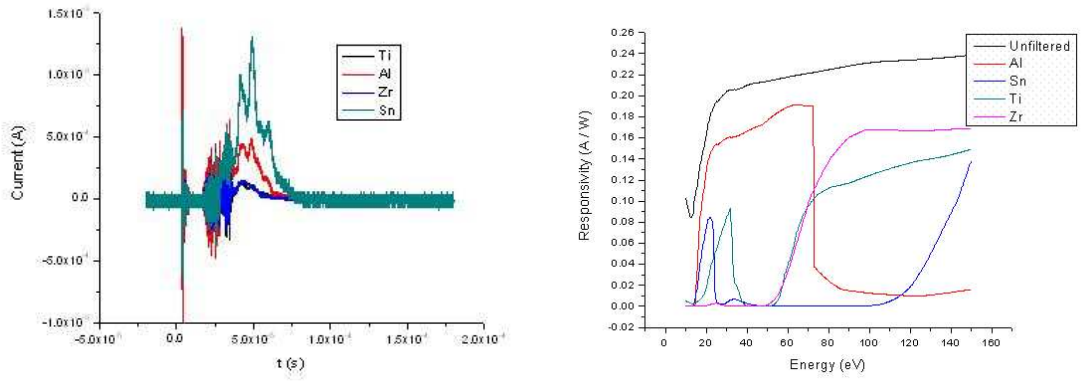

Fig. 32.— Left: Sample SXR raw data taken during a shot with counter-helicity merging. Right: SXR filter response functions.

= 85 μs as the VUV monochromator signal becomes weak; perhaps this phenomena becomes important approximately 30 μs earlier in the single spheromak case. If this hypothesis is correct, the VUV monochromator may not be a very useful temperature diagnostic for single spheromak shots, since it only sees the plasma for about 20 μs before the signal becomes too weak to be useful. A new current amplifier could help to alleviate this problem.

5.2. Results from SXR

Analysis of SXR data has led to progress in several important areas, but more work remains to be done. As mentioned previously, SXR could potentially allow us to measure the electron temperature for individual shots, while also providing a basis for comparison with the average temperature profiles derived from VUV monochromator data. The new filters installed last year (Al, Ti, Sn, and Zr) all produced measurable signals–an improvement upon previous incarnations of SXR for which data from one or more filters had to be thrown out due to low signal-to-noise ratios (9), (41).

Fig. 33.— SXR "lollipop" device. The large window is made of UV-fused silica (transmission cuts off abruptly above 7.3 eV, and the small window is sapphire (transmission cuts off above 8.3 eV). Once the device was installed in the machine, the windows were oriented at 90 degrees with respect to one another. Rotating the device then allowed us to position either window in the SXR line of sight.

5.2.1. Anomalous Tin Filter Signals

Temperature-fitting calculations were hindered by inexplicably strong signals from the tin-filtered diode in nearly all experimental runs. The left panel of Figure 32 shows SXR data from a typical shot. As was usually the case, the signal from the tin (Sn)-filtered diode for this shot was significantly stronger than the aluminum (Al) signal and at least five times as strong as the titanium (Ti) and zirconium (Zr) signals. We do not need PrismSPECT to tell us that this result is strange–simply look at the right panel of Figure 32. The Sn filter does not have the highest responsivity at any energy between 10 eV and 150 eV; it is dominated by the Al filter at low energies and by the Ti and Zr filters at high energies. It appears impossible that the Sn-filtered diode could show the strongest signal if all the filters were working

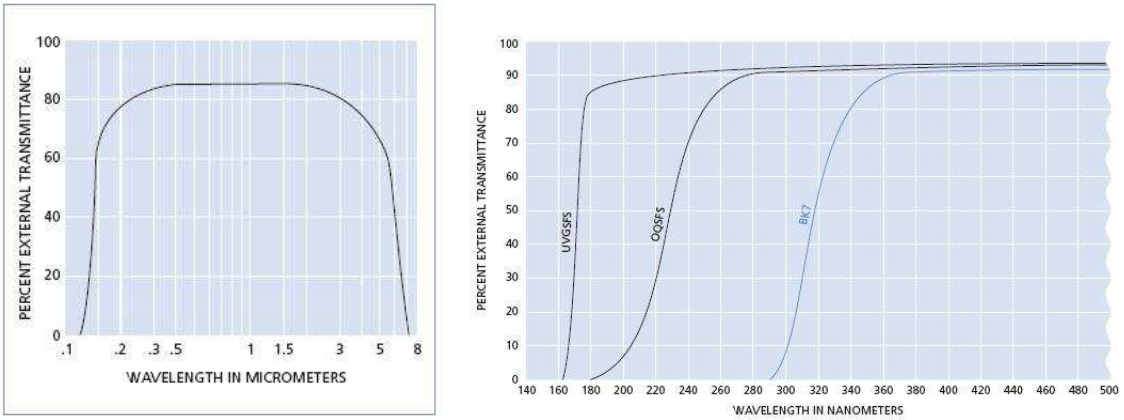

Fig. 34.— Left: Transmission function for 1 mm-thick uncoated sapphire. Right: Transmission function for UV-grade synthetic fused silica (UVGSFS). Ignore the OQSFS and BK7 curves. Note: $1\ eV = \frac{1239.8\ nm{\cdot}eV}{\lambda\ nm}$. Figures from (27) and (28).

correctly.

One possible explanation for the anomaly is that the Sn filter was passing photons at energies above 150 eV or below 10 eV. Given that the electron temperature in SSX is probably below 50 eV, we do not expect to see a significant flux of hard x-ray photons. High energy beams can be produced during magnetic reconnection, but exotic reconnection dynamics cannot explain the strong Sn signals because the anomaly was present in both single-spheromak and counter-helicity merging shots. Excess transmission in the UV was a more likely possibility. All four filters nominally have zero transmission below 10 eV, but even a small transmission rate by the Sn filter in the UV or visible might skew the data, since there are a plethora of strong emission lines from both hydrogen and impurity elements at these wavelengths.

In order to test the hypothesis that the Sn filter was passing photons with E $<$ 10 eV, we constructed a device that came to be known as the "lollipop" (shown in Figure 33). Its purpose was to block x-ray photons while still allowing UV and visible photons to reach SXR. This was accomplished by using windows made of UV-fused

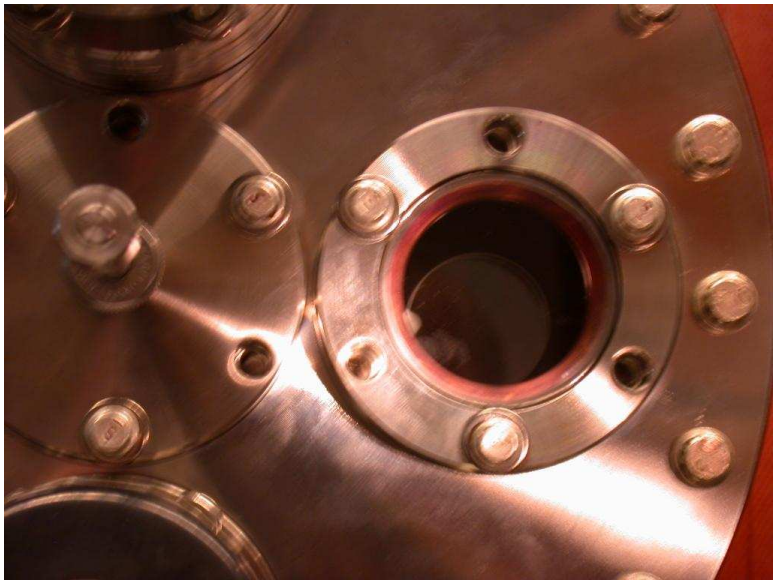

Fig. 35.— Photo of the "lollipop" device installed in the machine; the sapphire window is visible through the glass. SXR is connected to the flange just visible at the top of the image–in order to block it with the sapphire lens, all we had to do was rotate the shaft counterclockwise.

silica (UVFS) and sapphire. The transmittances of these materials cut off abrubtly just below 10 eV (see Figure 34), so they were ideal for identifying a UV or visible leak in the Sn filter. One window might have been sufficient, but by using two with slightly different transmission functions (UVFS cuts off above 7.3 eV, while sapphire cuts off above 8.3 eV), we hoped to garner additional information about the precise energies of the photons that were passing through the filters.

The device was inserted into SSX through the port directly below SXR. Once it was inside the machine, we loosened one of the screws and rotated the sapphire window 90 degrees. We could then position either window in the SXR line of sight by rotating the shaft of the lollipop.

Table 3 presents the results of the lollipop test. Signals from all four photodiodes with either of the windows in place were less than 2% of their unobscured values. The

Table 3: Mean filter signals from SXR lollipop test

Window Used	Al Signal (μA)	Sn Signal (μA)	Ti Signal (μA)	Zr Signal (μA)
No Window	210 ± 60	280 ± 70	40 ± 10	38 ± 9
UVFS	0.7 ± 0.1	3.2 ± 0.9	0.5 ± 0.1	0.3 ± 0.1
Sapphire	0.7 ± 0.2	4 ± 1	0.4 ± 0.2	0.4 ± 0.2

tin filter transmits more low-energy photons than any of the others, but the lollipop results show that the contribution to the overall tin signal by photons with E $<$ 8.3 eV is negligible. The signals obtained when using the UVFS and sapphire lenses differ by less than the experimental uncertainty for all filters, so it is also unlikely that the transmission by the tin filter increases rapidly as E approaches 10 eV.

Another possible cause of the anomalously high Sn signals was a tiny pinhole in the filter. Such a defect has been previously observed in SXR; it would cause the filter to indiscriminately pass photons of all wavelengths and therefore exhibit higher signals than expected. However, the negative results of the lollipop test rule out this possibility. We are therefore left with a mystery that is at present unsolved. Efforts to understand the observed Sn filter signals will continue–a good first step would be to exchange the filter currently in the machine for another [presumably] identical one–but for now we will proceed with electron temperature fitting using only data from the Al, Ti, and Zr-filtered diodes.

5.2.2. Electron Temperature Determination

The electron temperatures derived from fitting simulated filter ratios to SXR data are shown for several representative shots in Figure 36. The temperature profiles for individual shots feature no discernable pattern in the fluctations of T_e. However,

when we average over a number of counter-helicity shots (see Figure 37), there is a clear peak around t = 40 μs. The timing of this peak is in good agreement with estimates of the reconnection time based on time-of-flight calculations. Furthermore, Mach probe measurements by Horwitz (17) demonstrate a strikingly similar feature in the azimuthal bulk flow pattern. This corroborating evidence suggests that we are indeed observing heating from reconnection in the SXR data.

The magnitudes of the temperatures calculated using SXR are approximately 10 eV higher than those calculated from UV lines ratios, with counter-helicity temperatures peaking at 40-45 eV and single spheromak temperatures averaging approximately 30-35 eV. It is apparent that the single spheromak temperatures are only reliable in the interval t = 35-65 μs; at later times the filter signals become quite weak, and the resulting large fluctuations in the filter ratios prohibit any useful analysis. SXR has outperformed the VUV monochromator in this regard; while the monochromator signals become useless as early as t = 55 μs (see Figure 30), the SXR filter ratios remain consistent for an additional 10 μs. The early decay of the signals from both diagnostics is further evidence of the fact that FRCs have longer lifetimes than spheromaks.

Qualitative differences in the VUV monochromator (Figure 29) and SXR (Figure 37) temperature profiles beg the question: which measurement is more accurate? The relative simplicity of the line ratio measurements makes the monochromator result appealing; however, the SXR result is in better agreement with flow measurements. The temperatures shown in both Figures 29 and 37 are averaged over many shots, so the smoothing effects discussed in section 5.1.3 could be relevant in both cases. It should be noted that the appearance of a peak in T_e during counter-helicity shots is not a foregone conclusion. Magnetic reconnection may not be confined to a short interval in the middle of each shot; if the spheromak merging process were drawn out

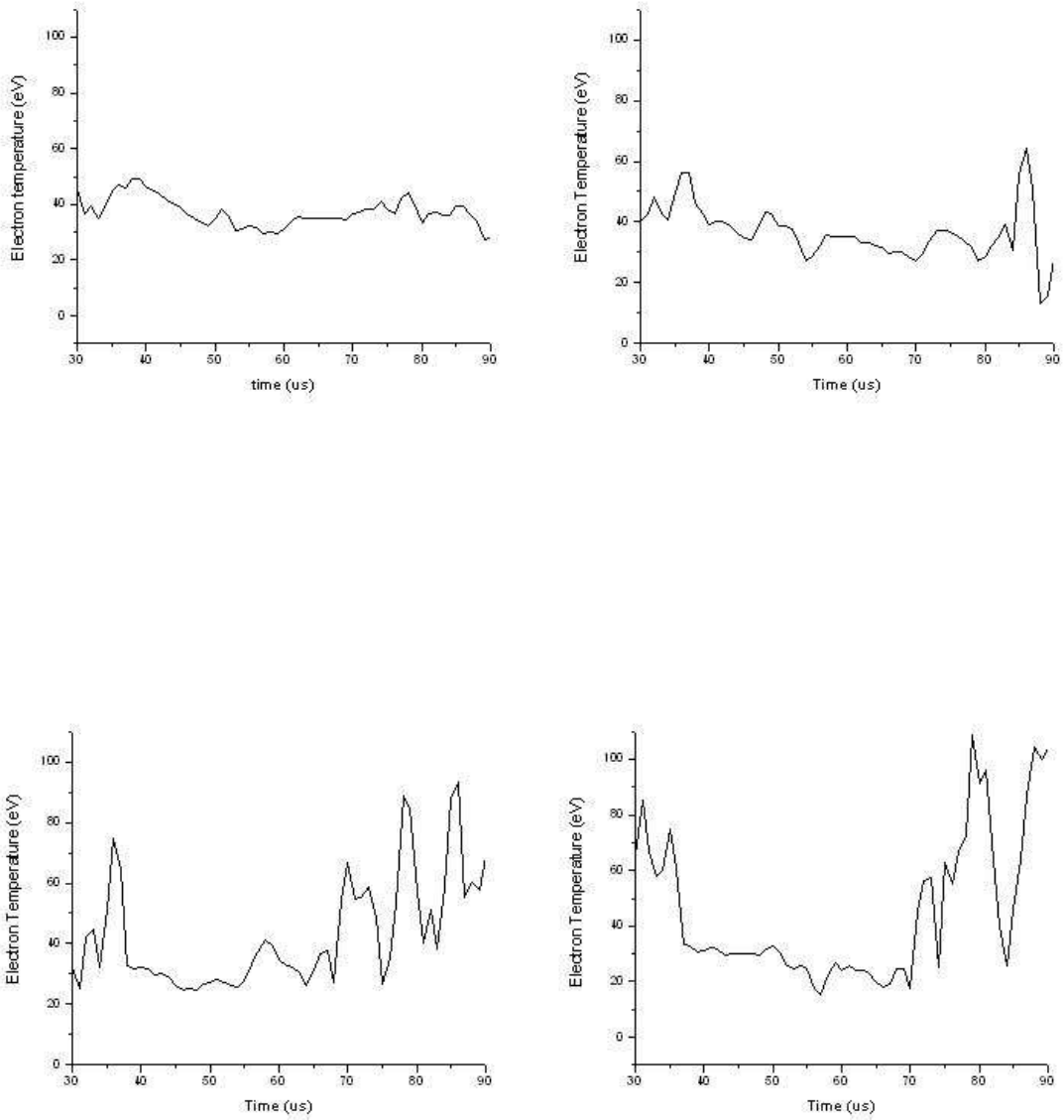

Fig. 36.— Temperatures derived from SXR filter ratios for two individual counter-helicity shots (top) and two single spheromak shots (bottom). The filter ratios used were Al/Ti, Al/Zr, and Ti/Zr, and a density of 5×10^{14} ions/cm^3 was assumed for comparison with PrismSPECT simulations.

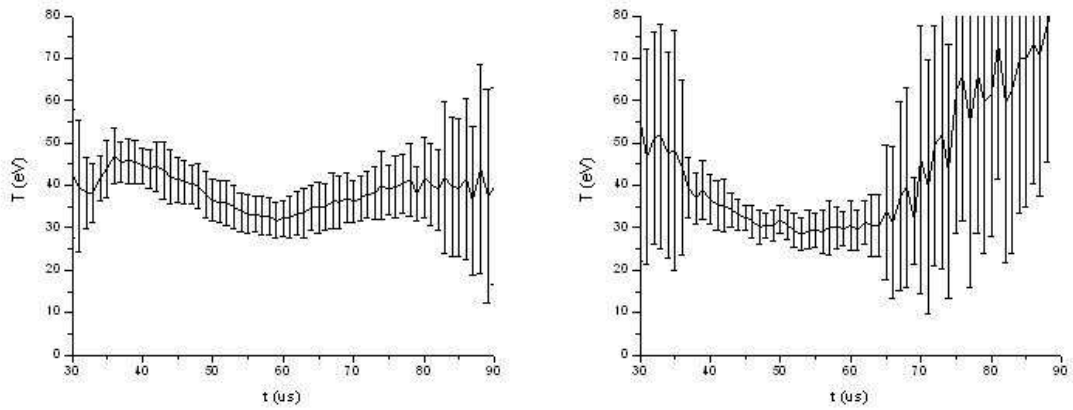

Fig. 37.— Average temperature profiles from 23 counter-helicity shots (left) and 23 single spheromak shots (right).

and less organized, the presence of reconnection would be manifested by higher overall temperatures during counter-helicity shots rather than by a peak in the temperature profile.

The discrepencies in the results will best be resolved through the collection of higher quality data with both diagnostics. SXR will be most useful when it is able to produce reliable temperature profiles for individual shots, as this is where its greatest advantage over the VUV monochromator lies. The temperature fitting process would be more tightly constrained if we could utilize a fourth filter signal; understanding the tin filter anomaly therefore remains a top priority. Further work will also involve a new set of PrismSPECT simulations featuring non-Maxwellian electron velocity distributions. We believe there may be a significant high-energy tail in the velocity distribution in SSX, so such a calculation may help our simulated spectra better match the actual emission by the plasma.

6. Summary and Conclusion

The VUV monochromator has been used in conjuction with PrismSPECT simulations to produce a number of new results. Four impurity emission lines were conclusively observed: C III 97.7 nm, C IV 155 nm, C III 229.7 nm, and O V 63.0 nm. Among these, the 155 nm line was by far the strongest, and the 229.7 nm line was anomalously strong in experiments compared to simulations and theoretical expectations. Similar results have been observed previously in SSX and in other spheromaks. The cause of this phenomenon remains to be determined. The non-detections of five other lines were just as valuable in our analysis of plasma composition. We have determined that the primary impurity in SSX is carbon, with oxygen also present at approximately 1/1000 of the carbon concentration.

Significant progress has been made in the analysis of the SSX electron temperature through the use of the 97.7 nm / 155 nm line ratio. Our latest calculations indicate an average electron temperature of 20 eV early in counter-helicity shots, increasing to 30-35 eV by t = 60-70 μs. The average temperature for single spheromak shots was approximately 20 eV. More data is needed for both counter-helicity merging and single spheromak shots; a third category of shot, co-helicity merging, should also be investigated.

Temperature-fitting calculations from SXR data and simulations have produced mixed results. Plagued with unreasonable signals from the tin-filtered diode, we have proceeded with calculations using only the other three filter signals. Typical electron temperatures were around 40-45 eV for counter helicity shots and 30-35 eV for single spheromak shots. These values were approximately 10 eV higher than the temperatures derived from VUV monochromator data, although the uncertainty ranges overlap at times.

The SXR temperature profile for counter-helicity merging peaks at t $\approx$ 40 μs and then decays afterwards; comparisons of this result with flow measurements from (17) suggest that the timing of the peak coincides with magnetic reconnection. However, SXR measurements cannot be considered truly reliable until we can identify the signature of reconnection in the temperature profiles of individual counter-helicity shots. VUV monochromator results show a later and more gradual rise in the plasma temperature during counter-helicity merging. This result could be accurate if reconnection is occurring haphazardly in space and time, resulting in relatively slow heating of the plasma rather than a rapid increase in T_e. Further work is needed to achieve agreement between the two diagnostics.

It should be noted that in our temperature calculations we have only scratched the surface of the problem's true complexity. For example, we have been assuming a spatially uniform temperature in the plasma, but this is almost certainly inaccurate (we might expect it to be hotter in the center, for instance). The line-of-sight nature of external measurements makes determining such structure difficult, but it should be possible to try several spatially varying models using Spect3D (37) and see which one best matches VUV monochromator or SXR observations.

Measurements of the electron temperature and impurity concentrations in SSX are vital for our understanding of magnetic reconnection and other processes in the plasma. As our knowledge of these variables improve, so will our ability to use SSX as a tool to gain insight into natural phenomena on the sun, in the earth's magnetosphere, and elsewhere in the universe. Given the difficulties involved in measuring a seemingly basic property such as temperature, it is no wonder that many of the details of plasma behavior remain unknown. However, the ingenuity required to tame this most energetic state of matter and the potential for new discovery are precisely what make plasma physics such an exciting field. The SSX team will continue to

work to fill the voids in our understanding of this important topic.

7. Acknowledgments

I'd like to thank my advisors, Michael Brown, David Cohen, and Chris Cothran, for giving me the opportunity to work on this exciting project and for providing invaluable guidance, support, and insight throughout the research process. Special thanks also go out to Joe MacFarlane at Prism Computational Sciences for his generous assistance with numerous aspects of the computer simulations. I'm indebted to all the students who have been part of the SSX team before me; their hard work and breakthroughs made my project possible. I have used a number of figures from previous SSX theses; however, all those that are not cited are my own. I've grateful to the Provost's office at Swarthmore College for funding my research through the Tarble Summer Research Fellowship.

A. Energy Level Diagrams for Impurity Ions

This appendix contains simplified Grotrian diagrams for several carbon, nitrogen, and oxygen ions. All wavelengths are given in nanometers. For lines with multiple components, the average wavelength of the components is given. Lines with wavelengths highlighted in bold were looked for with the VUV monochromator as part of this thesis project. The diagrams were compiled using (2) and (25).

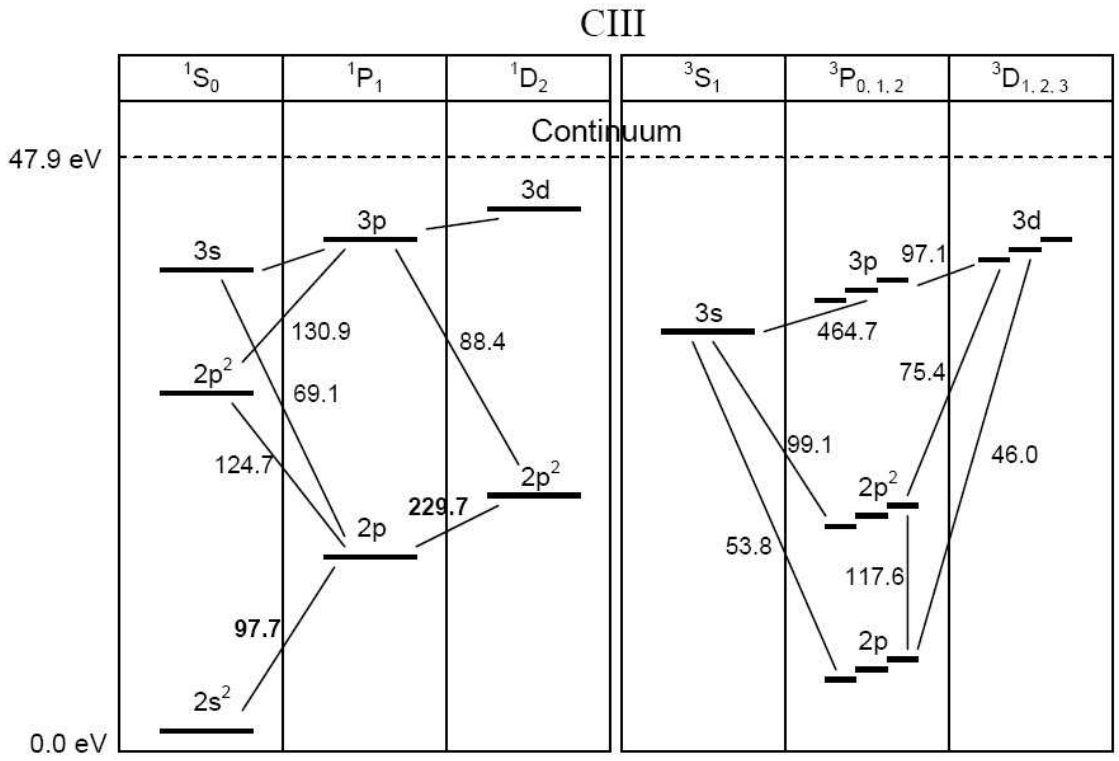

CIV

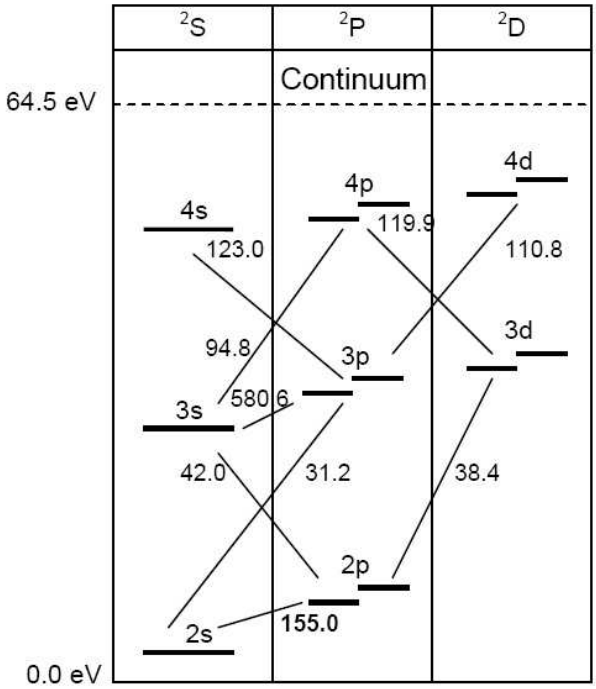
^{2}S
^{2}P
^{2}D
Continuum
64.5 eV
4s
4p
4d
3s
3p
3d
2s
2p
123.0
119.9
110.8
94.8
580.6
42.0
31.2
38.4
155.0
0.0 eV

CV

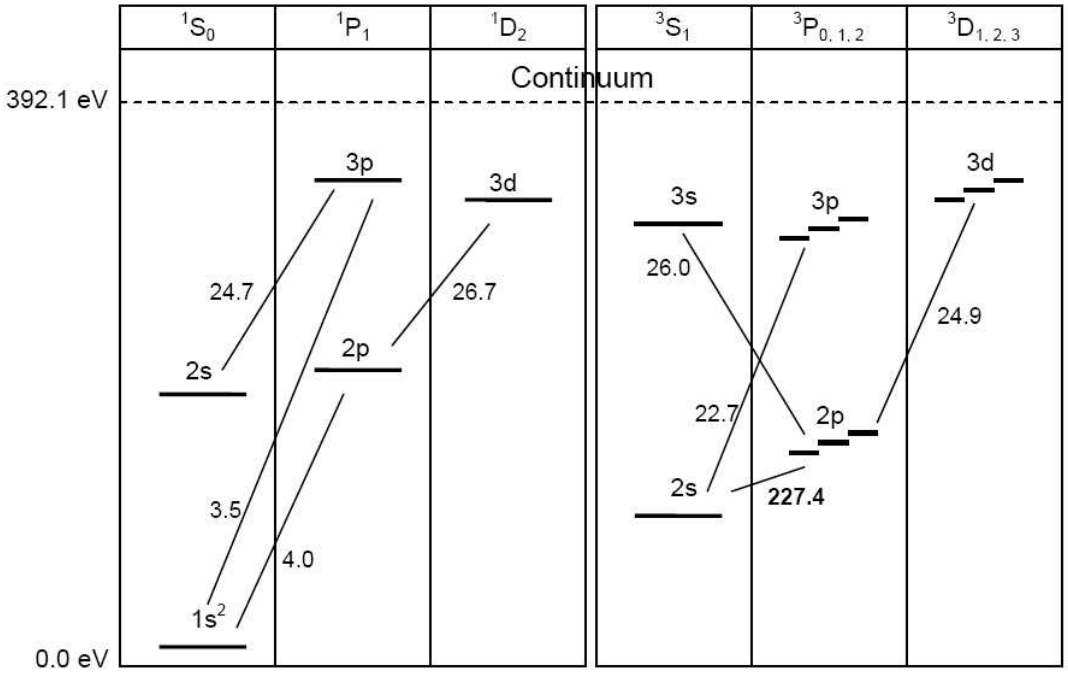
^{1}S$_0$
^{1}P$_1$
^{1}D$_2$
^{3}S$_1$
^{3}P$_{0,1,2}$
^{3}D$_{1,2,3}$
Continuum
392.1 eV
3p
3d
3s
3p
3d
2s
2p
2p
24.7
26.7
26.0
24.9
22.7
3.5
4.0
227.4
1s^2
2s
0.0 eV

NIV

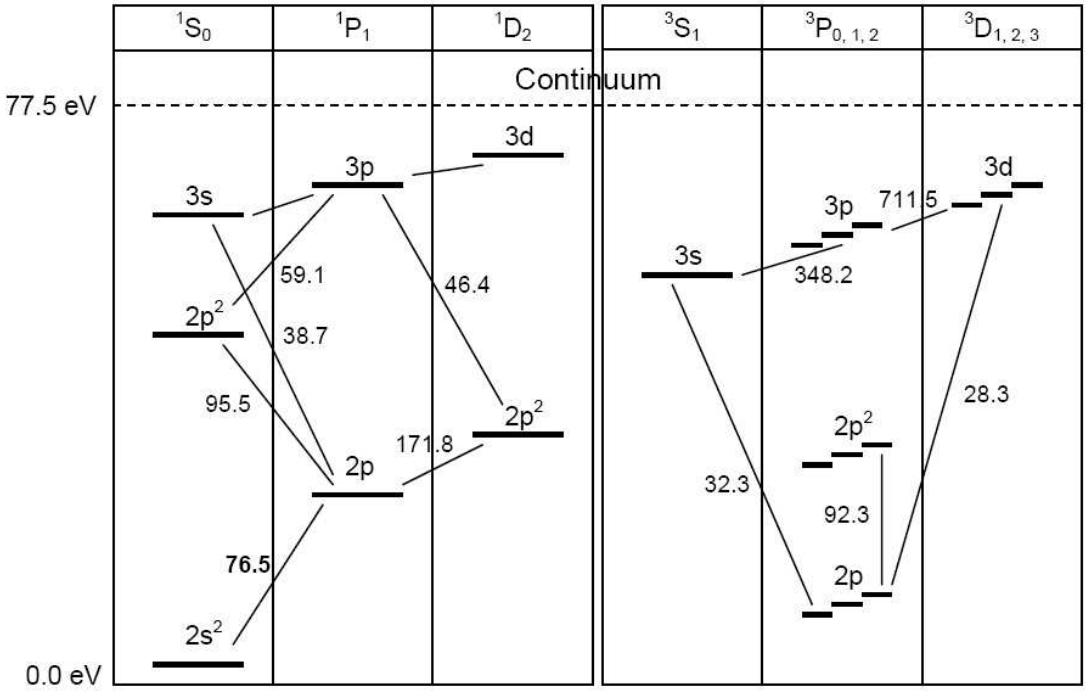
$^1S_0$
$^1P_1$
$^1D_2$
$^3S_1$
$^3P_{0,1,2}$
$^3D_{1,2,3}$
Continuum
77.5 eV
0.0 eV
3d
3p
3s
2p^2
2p
2s^2
59.1
46.4
38.7
95.5
171.8
76.5
711.5
348.2
28.3
32.3
92.3

NV

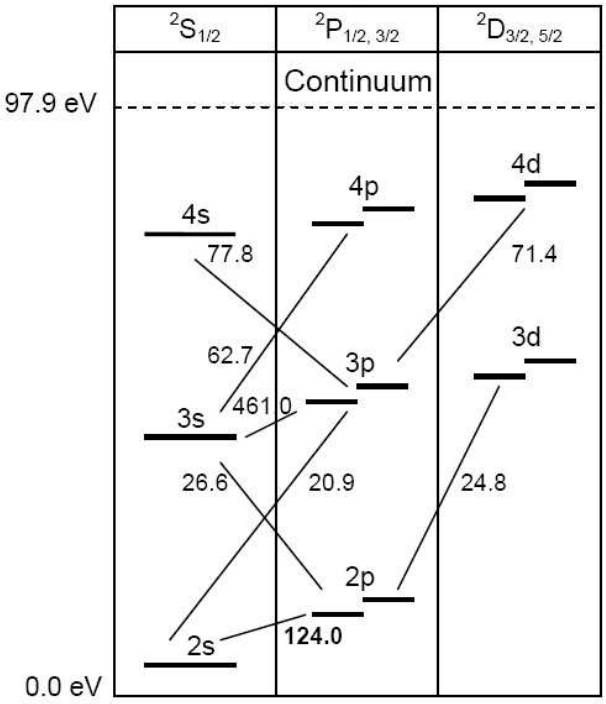
$^2S_{1/2}$
$^2P_{1/2,3/2}$
$^2D_{3/2,5/2}$
Continuum
97.9 eV
0.0 eV
4d
4p
4s
3d
3p
3s
2p
2s
77.8
71.4
62.7
461.0
26.6
20.9
24.8
124.0

OIV

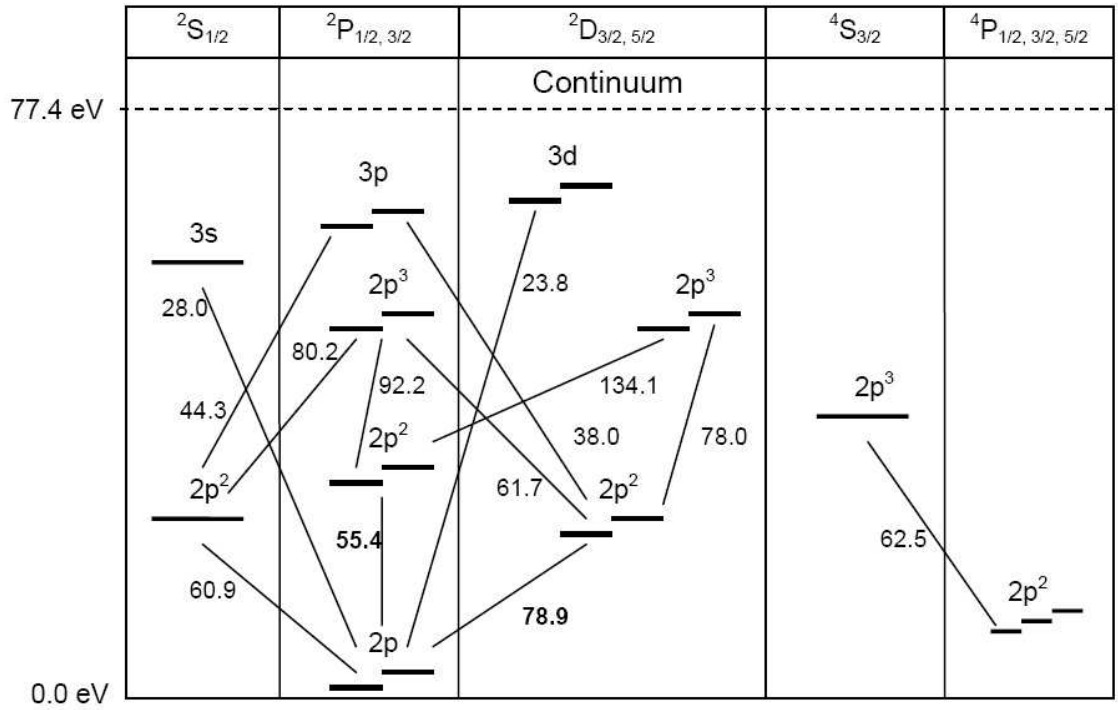
$^2S_{1/2}$
$^2P_{1/2, 3/2}$
$^2D_{3/2, 5/2}$
$^4S_{3/2}$
$^4P_{1/2, 3/2, 5/2}$
Continuum
77.4 eV
0.0 eV
3s
3p
3d
2p
$2p^2$
$2p^3$
28.0
44.3
80.2
92.2
55.4
60.9
23.8
61.7
38.0
134.1
78.0
78.9
62.5

OV

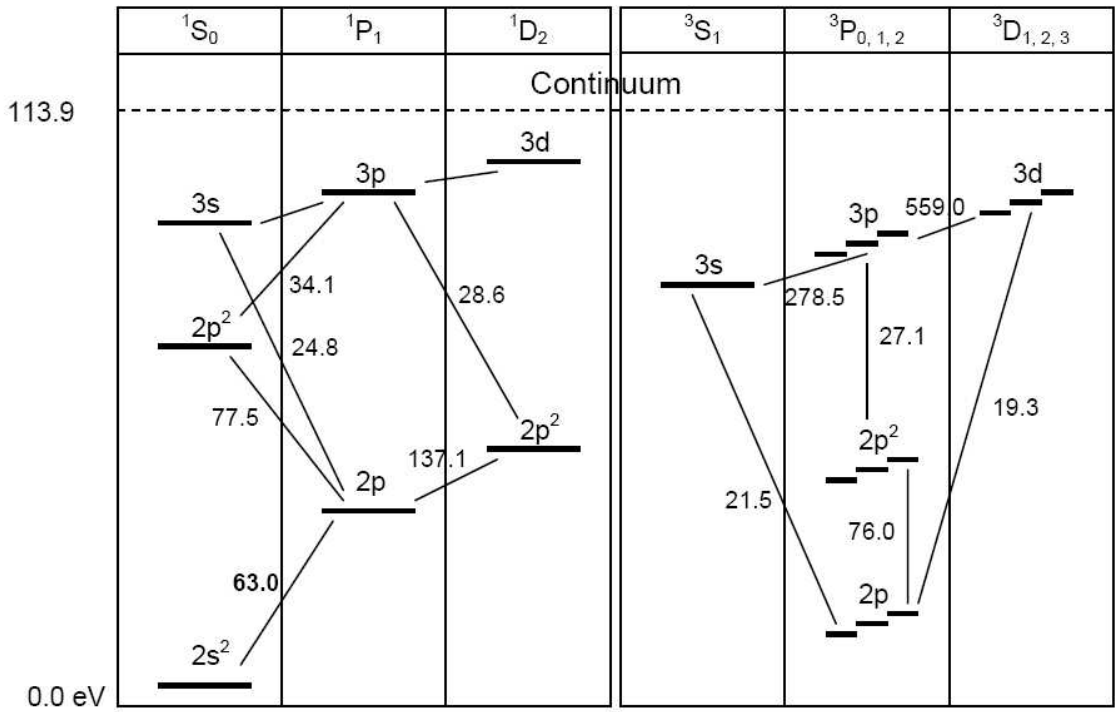
$^1S_0$
$^1P_1$
$^1D_2$
$^3S_1$
$^3P_{0, 1, 2}$
$^3D_{1, 2, 3}$
Continuum
113.9
0.0 eV
3s
3p
3d
2p
$2p^2$
$2s^2$
34.1
24.8
77.5
63.0
28.6
137.1
559.0
278.5
27.1
76.0
21.5
19.3

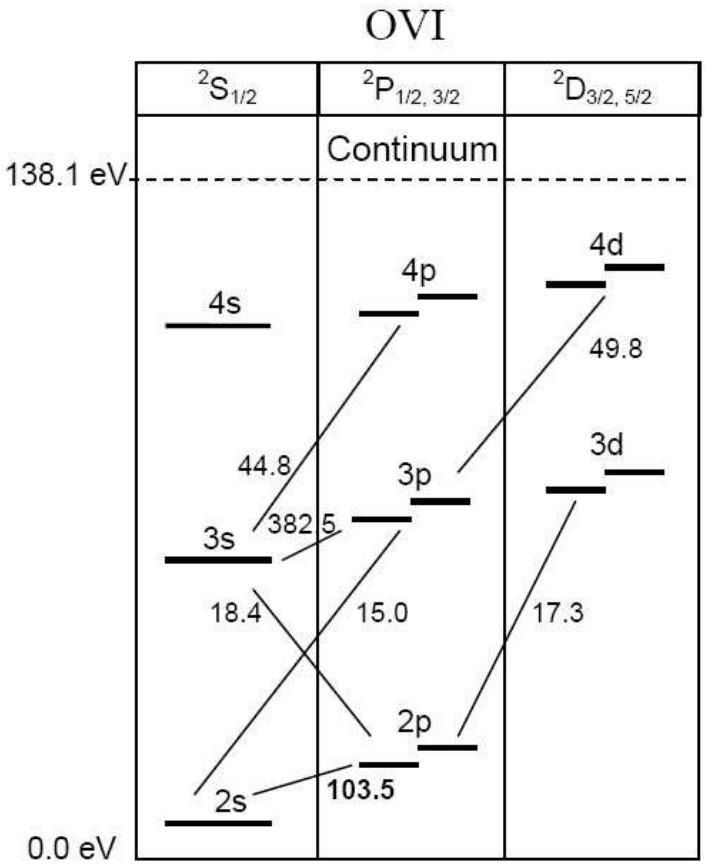
OVI
$^2S_{1/2}$
$^2P_{1/2, 3/2}$
$^2D_{3/2, 5/2}$
Continuum
138.1 eV
4d
4p
4s
49.8
3d
44.8
3p
382.5
3s
18.4
15.0
17.3
2p
103.5
2s
0.0 eV

B. Glossary

Alfvén Speed (v_A): The velocity at which large-scale, low frequency oscillations known as Alfvén waves travel in a plasma. The Alfvén speed acts as a sort of speed limit in the plasma.

Alfvén's Theorem (Frozen-in-Flux Theorem): In ideal MHD, the magnetic flux through a closed loop moving with the plasma is constant in time (the field lines are "frozen into" the plasma). This theorem is violated during magnetic reconnection.

Collective Behavior: Plasma dynamics are dominated by electromagnetic forces rather than by collisions between neutral particles.

Coronal Equilibrium: A state in which the electron density is too low for LTE, so that upward atomic transitions are assumed to be caused by collisions between electrons and ions, and downward transitions occur by spontaneous emission.

Debye Shielding: There are no large-scale electromagnetic fields in plasmas, because electrons tend to drift around positive ions, and they shield one another's electrical influence from the rest of the plasma.

External Measurements: Measurements made by detecting photons and energized ions emitted by the plasma. These can only produce volume of line-of-sight averaged values, so they integrate over any localized plasma structures.

Field-Reversed Configuration (FRC): A plasma configuration that results from the merging of two spheromaks with opposing helicities. The toroidal magnetic fields of the spheromaks annihilate during reconnection, so an ideal FRC has only a poloidal field.

Flux Conservers: Cylindrical copper containers within the SSX vacuum chamber that act as conducting boundaries to contain the plasma.

Internal Measurements: Measurements made by probes placed within the plasma. These produce precise measurements but only represent a small fraction of the total volume of the inhomogeneous plasma. They may also perturb the plasma and interfere with its properties.

Ion Doppler Spectroscopy (IDS): An external, photon-based diagnostic that allows one to infer ion flow velocity from emission line Doppler shifts and ion temperature from emission line Doppler broadening.

Magnetic Reconnection: A phenomenon that occurs when the magnetic field lines from two colliding plasma structures change their topology rapidly and merge, releasing stored magnetic energy in the form of heat or bulk motion.

Local Thermodynamic Equilibrium (LTE): A state in which collisional excitation and de-excitation are the dominant atomic processes. The electron density must be high enough that an ion in an excited state has a greater chance of returning to the ground state through collisional de-excitation than through spontaneous emission. LTE is distinguished from thermodynamic equilibrium in that the temperature need not be the same everywhere, and the emission spectrum is not a pure blackbody.

Lundquist Number (S): A special case of the Reynolds number that applies when the velocity in the formula for R_M is equal to the Alfvén speed. It measures how well the magnetic field lines are frozen into the plasma (in ideal MHD, S is infinite).

Magnetic Reynolds Number (R_M): A dimensionless quantity that describes the relative importance of the effects of convection versus diffusion on the magnetic field in a plasma.

Magnetohydrodynamics (MHD): A theory that uses a combination of fluid mechanics and classical electrodynamics to describe plasma behavior. In ideal MHD,

the plasma is assumed to be a perfectly conducting fluid.

Photomultiplier Tube (PMT): A device that converts the energy of a small number of photons into a measurable signal. Incoming photons strike a photocathode, causing electrons to be emitted through the photoelectric effect. These electrons are accelerated through a potential difference and strike a metal surface, which emits more electrons. The repetition of this process leads to a large amplification of the original signal.

Plasma: "A quasineutral gas of charged and neutral particles which exhibits collective behavior" (6).

Plasma Kinetic Theory: A theory used to analyze plasmas that relies on statistical mechanics. It is useful for low-density plasmas in which the infrequency of collisions between particles makes the assumptions of MHD invalid.

Poloidal: Refers to magnetic field lines or currents that pass through the center of a torus (i.e. through the donut hole).

PrismSPECT: A commercial software application that simulates radiative processes in plasmas, produces detailed spectra, and provides a collection of tools for analysis of properties such as ionization balance and line intensities.

Quasineutrality: A plasma is approximately neutral in any region because electrons tend to surround any local concentrations of positive charge (Debye shielding).

Soft X-Ray Detector (SXR): An external, photon-based SSX diagnostic that uses four photodiodes filtered by thin metal films to capture broad spectral information with high time resolution.

Spheromak: A donut-shaped plasma structure confined by its own toroidal and poloidal magnetic fields.

Stuffing Coil: During spheromak formation in SSX, current through these coils creates a magnetic field that is dragged along by the plasma as it leaves the gun and then reconnects to form the poloidal field of the spheromak.

Toroidal: Refers to magnetic field lines or currents that trace out circles around the axis of a torus-shaped plasma (for example, a spheromak or tokamak).

Vacuum Ultraviolet (VUV) Monochromator: An SSX diagnostic that measures the flux of photons emitted in a specific narrow wavelength band between 50 nm and 560 nm in real time.

REFERENCES

[1] Bai, T., "Solar Flare Forecasting," *Encyclopedia of Astronomy and Astrophysics*, ed. P. Murdin, Instititute of Physics Publishing, Philadelphia, 2000.

[2] Bashkin, S. and J. O. Stoner Jr., *Atomic Energy Levels and Grotrian Diagrams*, American Elsevier Publishing Company, Inc., New York, 1975.

[3] Blackman, E. G. and H. Ji, "Laboratory plasma dynamos, astrophysical dynamos, and magnetic helicity evolution," *Mon. Not. R. Astron. Soc.* **369**, 1837-1848 (2006).

[4] Brown, M. R., *Sweet-Parker reconnection: scaling for reconnection rates*, Swarthmore College.

[5] Brown, M. R., C. D. Cothran, and J. Fung, "Two fluid effects on three-dimensional reconnection in the Swarthmore Spheromak Experiment with comparisons to space data," *Phys. Plasmas* **13**,056503 (2006).

[6] Chen, F. F., *Introduction to Plasma Physics and Controlled Fusion, Volume 1: Plasma Physics*, Plenum Press, New York, second edition, 1984.

[7] Cothran, C. D., J. Fung, M. R. Brown, and M. J. Schaffer, "Fast high resolution echelle spectroscopy of a laboratory plasma," *Rev. Sci. Instrum.* **77**, 063504 (2006).

[8] Cunningham, G., "Impurities and impurity transport in the spheromak SPHEX," *Plasma Phys. Control. Fusion* **39** (1997) 1339-1354.

[9] Falk, A., "Dynamics of Field-Reversed Configuration in SSX," Senior Honors Thesis, Swarthmore College (2003).

[10] "Filter Transmission," *X-Ray Interactions with Matter*, Lawrence Berkeley National Laboratory, $http://www-cxro.lbl.gov/optical_constants/filter2.html$.

[11] Fung, J., "High Resolution Flow and Ion Temperature Measurements with Ion Doppler Spectroscopy at SSX," Senior Honors Thesis, Swarthmore College (2006).

[12] Funsten, H. O., S. M. Ritzau, R. W. Harper, and R. Korde, "Response of 100% Internal Carrier Collection Efficiency Silicon Photodiodes to Low-Energy Ions", *IEEE Trans. Nucl. Sci.* **48**, 6, December 2001.

[13] Griffiths, D. J., *Introduction to Electrodynamics*, Prentice Hall, Upper Saddle River, New Jersey, third edition, 1999.

[14] Gibson, K. J., S. J. Gee, and M. G. Rusbridge, "Ion energy measurements in the SPHEX spheromak," *Plasma Phys. Control. Fusion* **37** (1995) 31-41.

[15] Hokin, S., R. Fonck, and P. Martin, "A simple multifoil spectrometer for routine carbon and oxygen measurements," *Rev. Sci. Instrum.* **63** (10), October 1992.

[16] Holcomb, C. T., T. R. Jarboe, D. N. Hill, S. Woodruff, and R. D. Wood, "Sustained spheromak coaxial gun operation in the presence of an n = 1 magnetic distortion," *Phys. Plasmas* **13**, 022504 (2006).

[17] Horwitz, J., Senior Honors Thesis, Swarthmore College (2007).

[18] Jarboe, T. R. "Review of spheromak research," *Plasma Phys. Control. Fusion* **36** (1994) 945-990.

[19] Kato, Y., N. Satomi, M. Nishikawa, K. Watanbe, "Electron temperature measurement using the line-intensity ratio on the CTCC spheromak," *Plasma Phys. Control. Fusion* **35** (1993) 1513-1528.

[20] Khutoretsky, I. V., "Design of an optimal Ross filter system for x-ray spectra measurements in the range of 8.98-88 keV," *Rev. Sci. Instrum.* **66** (1), January 1995.

[21] Klimchuk, J. A. "On solving the coronal heating problem," *Solar Physics* **234** (2006) 41-77.

[22] Kulsrud, R. M., *Plasma Physics for Astrophysics*, Princeton University Press, Princeton, 2005.

[23] Kutner, M. L., *Astronomy: A Physical Perspective*, Cambridge University Press, New York, second edition, 2003.

[24] Landreman, M., "The Three-Dimensional Structure of Magnetic Reconnection in SSX," Senior Honors Thesis, Swarthmore College (2003).

[25] Lukin, V. S., Atomic Term Scheme Diagrams, Swarthmore College, 2000.

[26] Lukin, V. S., "Modeling SSX Spheromak Plasmas: Internal Physics from External Measurements," Senior Honors Thesis, Swarthmore College (2000).

[27] Melles Griot, "Material Properties: Sapphire," *www.mellesgriot.com/pdf/CatalogX/X_04_16.pdf*.

[28] Melles Griot, "Material Properties: Synthetic Fused Silica," *www.mellesgriot.com/pdf/CatalogX/X_04_11 − 13.pdf*.

[29] Mewe, R., "Atomic Physics of Hot Plasmas," *X-Ray Spectroscopy Astrophysics*, Eds. Jan van Paradijs and Johan A. M. Bleeker, Springer, Berlin, 1999.

[30] Murchadha, A. O., "Ion Temperature and Flow Velocity Measurements in SSX-FRC," Senior Honors Thesis, Swarthmore College (2005).

[31] Osterbrock, D. E., *Astrophysics of Gaseous Nebulae and Active Galactic Nuclei*, University Science Books, Mill Valley, CA, 1989.

[32] Ostlie, D. A. and B. W. Carroll, *An Introduction to Modern Stellar Astrophysics*, Addison-Wesley, San Francisco, second edition, 2007.

[33] Parker, E. N., "Sweet's Mechanism for Merging Magnetic Fields in Conducting Fluids," *J. Geophys. Res.* **62**, 509-520 (1957).

[34] Prism Computational Sciences, Inc., "AtomicModelBuilder Atomic Model Customization Tool," $www.prism-cs.com/Software/AtomicData/AtomicModelBuilder.htm$.

[35] Prism Computational Sciences, Inc., "Prism Atomic Data," $www.prism-cs.com/Software/AtomicData/AtomicData.htm$.

[36] Prism Computational Sciences, Inc., "PrismSPECT Spectral Analysis Code," $www.prism-cs.com/Software/PrismSPECT/PrismSPECT.htm$.

[37] Prism Computational Sciences, Inc., "Spect3D Imaging and Spectral Analysis Suite," $www.prism-cs.com/Software/Spect3D/Spect3D.htm$.

[38] Priest, E. and T. Forbes, *Magnetic Reconnection: MHD Theory and Applications*, Cambridge University Press, Cambridge, UK, 2000.

[39] Rybicki, G. B., and A. P. Lightman, *Radiative Processes in Astrophysics*, John Wiley & Sons, New York, 1979.

[40] Soukhanovskii, V. A., D. Stutman, M. Iovea, M. Finkenthal, H. W. Moos, T. Munsat, B. Jones, D. Hoffman, R. Kaita, and R. Majeski, "Multilayer mirror and foil filter AXUV diode arrays on CDX-U spherical torus," *Rev. Sci. Instrum.* **72**, 1 (2001).

[41] Swisher, V., "Modeling UV and X-ray Spectra from the Swarthmore Spheromak Experiment," Senior Thesis, Swarthmore College (2006).

[42] Thorne, A., U. Litzén, S. Johansson, *Spectrophysics: Principles and Applications*, Springer, Berlin, 1999.

[43] Turner, W. C., G. C. Goldenbaum, E. H. A. Granneman, J. H. Hammer, C. W. Hartman, D. S. Prono, J. Taska, "Investigations of the magnetic structure and the decay of a plasma-gun-generated compact torus," *Phys. Fluids* **26** (7), July 1983.

[44] Wang, H. "Solar Flare Magnetic Fields," *Encyclopedia of Astronomy and Astrophysics*, ed. P. Murdin, Instititute of Physics Publishing, Philadelphia, 2000.